The thermo-viscous fingering instability of a cooling spreading liquid dome

Ghanim Algwauish (غانم الغويش)[1, a)] and Shailesh Naire (शैलेश नायर)[2, b)]

[1)] *Department of Mathematics, University of Mosul, Mosul, Iraq, 41002*

[2)] *School of Computer Science and Mathematics, Keele University, ST55BG, United Kingdom*

(Dated: October 25, 2023)

We investigate a theoretical model of a molten viscous planar liquid dome spreading under gravity over an inclined substrate. The liquid in the dome cools as it spreads, losing its heat to the surrounding colder air and substrate. Coupled nonlinear evolution equations for the dome's thickness and temperature describing the spreading flow are derived employing the lubrication approximation. The coupling between the flow and cooling is via a temperature-dependent viscosity. For intermediate Péclet numbers, a new one-dimensional free surface shape is identified. In this solution, the hotter and more mobile liquid piles up behind the dome's colder and less mobile leading edge, forming a distinct elevated ridge at the flow front. The ridge solution is mapped in parameter space. The transverse stability of the one-dimensional ridge solution is investigated using linear stability analysis and numerical simulations. The existence of a thermo-viscous fingering instability is revealed. For this instability to occur the presence of the ridge is shown to be necessary. Two-dimensional simulations confirm the stability analysis elucidating the underlying thermo-viscous mechanism.

I. INTRODUCTION

The slow viscous spreading of a mass of liquid is ubiquitous in a wide range of problems[1,2]. It has many important applications in chemical engineering, such as in coating flows[3], in pancake making and surface coating applications[4], and in the spreading of reactor core melt in nuclear engineering[5]. It also occurs in many geophysical and environmental scenarios, such as in lava[6] and glacier[7] flows, and in mudslides[8]. In these large-scale geophysical and environmental flows, and in some heavy-duty industrial coating flows, spreading is gravity-driven causing the liquid to flow down the underlying surface resisted by the viscous forces of the liquid, commonly referred to as a viscous-gravity current[9].

The isothermal spreading of viscous-gravity currents is well studied both experimentally and theoretically[1,2]. In comparison, fewer studies have considered non-isothermal spreading. This is a complex scenario involving the spreading of a molten liquid undergoing cooling via heat loss to the colder overlying air and underlying substrate. This is relevant in many flow scenarios, such as in lava[6], high-temperature corium melt[5], molten metal coating (e.g., in spray metallizing for marine coatings[10]) and making of pancakes[4]. The coupling between the flow and the transfer of heat energy presents challenges from both experimental and theoretical perspectives. For instance, the extent of cooling may lead to variations in flow rheology. Viscosity variations in temperature can be quite significant[11]; flows may exhibit non-Newtonian behaviour due to changes in flow composition as a result of cooling[6,12]; under certain conditions phase change at the flow surface could result in solidification and formation of a surface crust[6]. Conversely, the flow convects the heat causing cooling. The interplay between the flow and cooling results in a variety of dynamic flow patterns, such as the flow front branching in a fingering-type instability, e.g., advancing *pahoehoe* lava flow fronts develop toe-shaped protrusions[6]. A common theme in these flow scenarios is that these spatial instabilities are unwanted. A fingering instability can prevent uniform coating of a molten metal on a substrate in spray metallizing[10] or in making a pancake of uniform thickness[4]; branching of lava flows enhances its spreading, which can be hazardous and can cause damage to infrastructure and buildings; similarly with the spreading of core melt in a nuclear reactor accident. These behaviours have motivated analysts to investigate the interplay between the spreading flow and cooling in order to better understand the mechanisms driving fluid instabilities and develop strategies on how to control or eliminate them.

It is important to note previous studies that have investigated fingering instabilities in isothermal flow using fluids of different viscosities along the flow direction. Although this flow scenario does not capture the thermo-viscous coupling, nevertheless, these studies provided the basic mechanism underlying the fingering instabilities observed in such flows. The classical work by Saffman & Taylor[13] identified the existence of a viscous fingering instability in confined porous media flow involving a less viscous fluid displacing a more viscous fluid. Recently, Kowal[14] demonstrated that the viscous fingering instability is also observed in the isothermal flow of an unconfined viscous-gravity current involving a longitudinal viscosity contrast between two fluids, referred to as a viscous banding instability. The instability is shown to exist when a less viscous fluid intrudes into a band of more viscous fluid. The key driving mechanism is a jump in the hydrostatic pressure gradient across the intrusion front which manifests as a discontinuity in the free surface slope there. The instability is shown to be stabilized by buoyancy forces at large transverse wavenumbers.

[a)] g.m.abdullah@uomosul.edu.iq

[b)] s.naire@keele.ac.uk; Corresponding author

Sansom *et al.*[15,16] were the first to investigate the thermo-viscous effect on the dynamics of a spreading cooling viscous-gravity current. They considered spreading on a horizontal substrate using three temperature-dependent viscosity models (linear, exponential and bi-viscosity). Their results showed free surface profiles with a steep flow front followed by a central plateau (the pancake-shaped profile). This is due to preferential cooling of fluid near the flow front which forms a barrier, forcing the height at the front to grow as hot, less viscous fluid continues to be fed in behind the front. They also showed that, when the coupling between the viscosity and temperature was strong and sufficient cooling produced a significant viscosity contrast along the flow front, then transverse perturbation to the flow front can become unstable leading to a fingering instability.

The non-isothermal spreading of a viscoplastic dome on a horizontal plane was investigated by Balmforth and Craster[17]. Solutions were obtained for the growth of a vertically isothermal lava dome in the asymptotic limit of low reduced Péclet number. They also considered the development of non-axisymmetric domes and used the thin layer model to explore the possibility of fingering-type instabilities. Balmforth, Craster, and Sassi[18] extended this study to allow the reduced Péclet number to be $O(1)$. They described solutions that illustrate the dynamics of an expanding Bingham fluid with a temperature-dependent viscosity. A key feature (also noted in the PhD thesis of Sansom[19]) is that liquid near the flow front gets cooler and less mobile and is then overridden as the hot and more mobile fluid expands, creating a so-called *collar* of cold liquid. Two reduced models that approximate the temperature equation: a vertically isothermal theory (similar to Balmforth and Craster[17]), and a *skin theory* are compared to the $O(1)$ reduced Péclet number numerical simulations.

The seminal works by Sansom *et al.*[15,16] and Balmforth *et al.*[17,18], have contributed significantly in developing the theoretical framework to investigate non-isothermal aspects of these flows. However, their studies were confined to spreading over a horizontal substrate. In this work, we demonstrate that the inclination of the substrate, under certain conditions, can further enhance the mobility of the hot and less viscous liquid behind the cooler and less mobile flow front, resulting in the piling-up of the liquid there and subsequently forming an elevated *fluid ridge*. This feature is absent in non-isothermal spreading flows over a horizontal substrate. Moreover, we also demonstrate that the thermo-viscous instability mechanism postulated in the previous studies could be reinforced in the presence of the ridge, resulting in it losing its stability to transverse perturbations. Such an instability could be a precursor to the fingering instabilities observed in such flows. The absence of this feature in spreading flows over a horizontal substrate may have contributed to why these studies have simulated only weak (very small growth rate) fingering instabilities using this configuration.

Based on the above considerations, the goal of this paper is twofold: firstly, to include the effect of substrate inclination, and to delineate the domain of existence of the fluid ridge in parameter space. Secondly, to investigate the transverse stability of the fluid ridge solution to small-amplitude variations in the thickness and temperature. The plan of the paper is as follows. In §II we extend the models by Sansom *et al.* and Balmforth *et al.* to include the horizontal component of gravity arising due to the inclination of the substrate. The existence of the fluid ridge is shown via numerical solutions of the evolution equation in §III. In §IV, we characterize the ridge solution and show its existence in parameter space (Fig. 5). The stability of the ridge solution is considered using a linear stability analysis in §V A and numerical simulations in §V B. In §VI, we provide concluding remarks and outline future work.

II. MATHEMATICAL MODEL

We follow the modelling framework developed in previous related studies[15,18]. Consider a dome of hot liquid at initial temperature T_e^* spreading under the influence of gravity down a colder inclined substrate at temperature T_s^*, as shown in Fig. 1. Hot liquid at constant temperature T_e^* and time-dependent flux $Q_s^*(t^*)$ is introduced into the dome through a source at a specified location on the substrate (see Fig. 1). The substrate is inclined at an angle β to the horizontal.

We introduce a planar Cartesian coordinate system (x^*, y^*, z^*) with the x^*, y^*-axes along the plane, the z^*-axis normal to the plane and the origin is fixed at the location of the source, as shown in Fig. 1. We denote the free surface of the dome (the air-liquid interface) as $z^* = h^*(x^*, y^*, t^*)$. The characteristic dome height, H^*, is assumed to be much smaller than the typical length scale, L^*, in the flow direction.

We assume that the liquid in the dome is Newtonian with constant properties, except, the liquid viscosity is dependent on the temperature. The flow within the dome is assumed to be slow and viscous dominated. The liquid in the dome loses its heat via the colder free surface exposed to the colder air at temperature T_a^* assumed constant external to the liquid dome, and substrate at $z^* = 0$ at constant temperature $T_s^* < T_e^*$. We do not consider phase transition associated with solidification due to cooling near the surface or substrate. T_a^* and T_s^* are assumed to be much higher than the melting point to prevent the dome from solidifying. We also assume that the plane is pre-wetted with a thin precursor layer with the same liquid as in the dome, of constant thickness H_b^*, with $H_b^* \ll H^*$. We note that this layer is a mathematical regularization to avoid the contradiction between applying the no-slip boundary condition at the fluid-solid interface and the motion of the contact lines at the dome's edges, referred to as "contact line paradox". This approach is appropriate even if the substrate

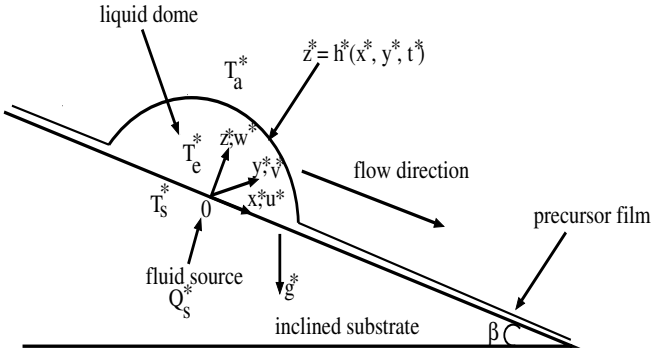

Figure 1: Sketch of a hot liquid dome spreading down on a colder inclined plane.

is dry but the liquid is completely wetting, as long as $H_b^* \ll H^*$.

A. Governing Equations and boundary conditions

The governing equations are given by the conservation of mass and momentum,

$$\nabla^* \cdot \boldsymbol{u}^* = 0, \tag{1a}$$

$$\boldsymbol{u}^*_{t^*} + \boldsymbol{u}^* \cdot \nabla^* \boldsymbol{u}^* = -\frac{1}{\rho^*}\nabla^* p^* + \nabla^* \cdot \boldsymbol{\tau}^* + \boldsymbol{g}^*, \tag{1b}$$

where ρ^* is the liquid density (assumed constant), $\boldsymbol{\tau}^*$ denotes the liquid viscous stresses, $\boldsymbol{u}^* = (u^*, v^*, w^*)$ denote the components of the liquid velocity in the x^*, y^* and z^* directions, respectively, p^* is the pressure in the liquid, $\nabla^* = (\frac{\partial}{\partial x^*}, \frac{\partial}{\partial y^*}, \frac{\partial}{\partial z^*})$ and $\boldsymbol{g}^* = g^*(\sin\beta, 0, -\cos(\beta))$, where g^* is the acceleration due to gravity and β is the angle of inclination of the substrate. The constitutive relation between the liquid stress and its rate of strain for a Newtonian liquid is written as:

$$\boldsymbol{\tau}^* = \mu^*(T^*)\dot{\boldsymbol{\gamma}}^*, \tag{2}$$

where μ^* is the liquid viscosity, $\dot{\boldsymbol{\gamma}}^*$ is the rate of strain tensor and T^* is the temperature.

The energy equation governing the temperature, T^*, is given by:

$$\rho^* c_p^* \left[T^*_{t^*} + \boldsymbol{u}^* \cdot \nabla^* T^*\right] = \kappa^* \nabla^{\star 2} T^*, \tag{3}$$

where c_p^* is the specific heat of the liquid (assumed constant), κ^* is its thermal conductivity (assumed constant) or alternatively the liquid's thermal diffusivity is $\kappa_d^* = \kappa^*/(\rho^* c_p^*)$. We neglect viscous heating effects.

The viscosity increases as temperature decreases. We use an exponential viscosity decay model to describe this relationship, given by:

$$\mu^*(T^*) = \mu^*_{min} + (\mu^*_R - \mu^*_{min})e^{-\alpha^*(T^* - T^*_R)}, \tag{4}$$

where T_R^* is a reference temperature, μ_R^* is the viscosity at the reference temperature, μ^*_{min} is a minimum viscosity limit and α^* is a temperature decay constant. This viscosity-temperature relationship is applicable for various types of lava[11]. Other temperature-viscosity relationships considered in the literature include a bi-viscosity model[15,20]. It can be written as: $\mu^* = \mu_e^*$, if $T^* > T_m^*$ and $\mu^* = \mu_a^*$, otherwise, where $\mu_a^* = \mu^*(T_a^*)$, $\mu_e^* = \mu^*(T_e^*)$ (with $\mu_a^* > \mu_e^*$) and T_m^* ($T_a^* < T_m^* \leq T_e^*$) is a fixed temperature in the solidus-liquidus transition. This relationship is a proxy of a nearly solidified layer characterised by a higher viscosity. In this paper, we only report results using the exponential viscosity model which is adequate to describe the basic underlying instability mechanism reported here.

We impose the no-slip boundary condition for the velocity field at the surface of the plane $z^* = 0$, with the flow speed from the source given by $w_s^*(x^*, y^*, t^*)$ taken as a vertical velocity. Therefore $u^* = 0$, $w^* = w_s^*(x^*, y^*, t^*)$ at $z^* = 0$. Assuming well-developed Poiseuille flow through this vent (assumed rectangular between $|x^*| \leq x_0^*, |y^*| \leq y_0^*$, where $(x, y)_0^*$ is the half-width of the source), with liquid flux, Q_s^*, w_s^* is approximated as:

$$w_s^* = \frac{9Q_s^*(t^*)}{16 x_0^* y_0^*}\left[1 - \left(\frac{x^*}{x_0^*}\right)^2\right]_+ \left[1 - \left(\frac{y^*}{y_0^*}\right)^2\right]_+, \tag{5}$$

where the subscript + denotes the positive part when $(x^*, y^*) \leq (|x_0^*|, |y_0^*|)$, and zero otherwise.

The heat transfer at the free surface, $z^* = h^*(x^*, y^*, t^*)$ and the substrate, $z^* = 0$ is assumed to follow Newton's law of cooling. Using this, the boundary condition at the substrate, $z^* = 0$, is[18]:

$$\begin{aligned}\kappa^* T^*_{z^*} =& \rho^* c_p^*(T^*(x^*, y^*, 0, t^*) - T_e^*)w_s^* \\ &+ b_s^*(T^*(x^*, y^*, 0, t^*) - T_s^*),\end{aligned} \tag{6}$$

where b_s^* is a heat transfer coefficient (assumed constant). The first term on the right represents the convective heat transfer from the vent into the bulk liquid and the second term on the right is the Newton cooling to the substrate. Similarly, on the free surface, $z^* = h^*(x^*, y^*, t^*)$, we have[18]:

$$-\kappa^*(\mathbf{n}^* \cdot \nabla^* T^*) = a_m^*(T^*(x^*, y^*, h^*, t^*) - T_a^*), \tag{7}$$

where a_m^* is a heat transfer coefficient at the free surface and T_a^* is the ambient temperature. The first term on the right is the Newton cooling to the surrounding air.

Taking the pressure of the liquid in the dome relative to the air pressure and neglecting surface tension, the normal stress at the air-liquid interface is written as:

$$(-p^* \boldsymbol{I} + \boldsymbol{\tau}^*) \cdot \mathbf{n}^* = 0, \quad \text{at} \quad z^* = h^*(x^*, y^*, t^*), \tag{8}$$

where, $\mathbf{n}^* = \frac{\nabla^*(z^* - h^*(x^*,t^*))}{|\nabla^*(z^* - h^*(x^*,t^*))|} = \frac{1}{\sqrt{1 + h^{\star 2}_{x^*} + h^{\star 2}_{y^*}}}\left(-h^*_{x^*}, h^*_{y^*}, 1\right)$, is the unit outward normal to the free surface $z^* = h^*(x^*, y^*, t^*)$. The corresponding tangent vectors to the free surface in the x^* and y^* directions are given by $[\mathbf{t}_x^*, \mathbf{t}_y^*] = \frac{1}{\sqrt{1 + h^{\star 2}_{x^*} + h^{\star 2}_{y^*}}}\left[(1, 0, h^*_{x^*}), (0, 1, h^*_{y^*})\right]$,

respectively. Using these, we can write the normal and two tangential components of Eq. (8) as

$$\frac{1}{\sqrt{1+h_{x^*}^{\star 2}+h_{y^*}^{\star 2}}}[-2h_{x^*}^*\tau_{zx}^*-2h_{y^*}^*\tau_{yz}^*+2h_{x^*}^*h_{y^*}^*\tau_{xy}^* + \tau_{zz}^*+h_{x^*}^{\star 2}\tau_{xx}^*+h_{y^*}^{\star 2}\tau_{yy}^*]=p^*, \tag{9a}$$

$$h_{x^*}^*(\tau_{zz}^*-\tau_{xx}^*)+\tau_{xz}^*(1-h_{x^*}^{\star 2})-h_{x^*}^*h_{y^*}^*\tau_{yz}^*-h_{y^*}^*\tau_{xy}^*=0, \tag{9b}$$

$$h_{y^*}^*(\tau_{zz}^*-\tau_{yy}^*)+\tau_{yz}^*(1-h_{y^*}^{\star 2})-h_{x^*}^*h_{y^*}^*\tau_{xz}^*-h_{x^*}^*\tau_{xy}^*=0. \tag{9c}$$

The kinematic condition at the free surface $z^* = h^*(x^*, y^*, t^*)$ is based on this being a material surface so that fluid particles which lie on the surface must always remain on the surface. This implies that $\frac{D}{Dt}[z^* - h^*(x^*, y^*, t^*)] = 0$. This can be written as:

$$h_{t^*}^*+u^*h_{x^*}^*+v^*h_{y^*}^*=w^*. \tag{10}$$

B. Nondimensionalisation of the governing equations and boundary conditions

We define an aspect ratio $\epsilon = H^*/L^* \ll 1$. Also, $U^* = (\rho^* g^* H^{*^3})/(\mu_R^* L^*)\cos\beta$, is a typical flow speed in the x^* and y^*-direction which is derived by balancing the horizontal liquid pressure gradient $(\rho^* g^* \cos\beta/L^*)$ with the liquid viscous shear stress $(\mu_R^* U^*/H^{*^2})$, μ_R^*, is a reference viscosity. The pressure is measured using a characteristic scale $P^* = \rho^* g^* H^* \cos\beta$ (the hydrostatic pressure). We introduce the following dimensionless variables:

$$\begin{aligned}
&(x^*, y^*) = L^*(x, y), \quad (z^*, h^*) = H^*(z, h), \\
&(u^*, v^*, w^*) = (U^*u, U^*v, \epsilon U^*w), \quad p^* = P^\star p, \\
&\tau^* = \mu_R^*\left(\frac{U^*}{H^*}\right)\tau, \quad \dot{\boldsymbol{\gamma}}^* = \left(\frac{U^*}{H^*}\right)\dot{\boldsymbol{\gamma}}, \quad \mu^* = \mu_R^*\mu, \\
&\theta = \frac{(T^*-T_a^*)}{(T_e^*-T_a^*)}, \quad t^* = (L^*/U^*)t.
\end{aligned} \tag{11}$$

The dimensionless equations for the flow and energy can be written as:

$$u_x + v_y + w_z = 0, \tag{12a}$$

$$\epsilon^2 Re\,[u_t + uu_x + vu_y + wu_z] = -p_x + S + \epsilon\partial_x\tau_{xx} + \epsilon\partial_y\tau_{xy} + \partial_z\tau_{xz}, \tag{12b}$$

$$\epsilon^2 Re\,[v_t + uv_x + vv_y + wv_z] = -p_y + \epsilon\partial_x\tau_{yx} + \epsilon\partial_y\tau_{yy} + \partial_z\tau_{yz}, \tag{12c}$$

$$\epsilon^4 Re\,[w_t + uw_x + vw_y + ww_z] = -p_z - 1 + \partial_x\epsilon^2\tau_{zx} + \epsilon^2\partial_y\tau_{zy} + \epsilon\partial_z\tau_{zz}, \tag{12d}$$

$$\epsilon^2 Pe\,[\theta_t + u\theta_x + v\theta_y + w\theta_z] = \epsilon^2\theta_{xx} + \epsilon^2\theta_{yy} + \theta_{zz}. \tag{12e}$$

The nondimensionalised constitutive relation between the liquid stress and its rate of strain for a Newtonian liquid is written as:

$$\boldsymbol{\tau} = \mu(\theta)\dot{\boldsymbol{\gamma}}. \tag{13}$$

The exponential viscosity-temperature model in dimensionless form is written as:

$$\mu(\theta) = \mu_{min} + (1-\mu_{min})e^{-\alpha\theta}. \tag{14}$$

The dimensionless strain rate tensor becomes

$$\dot{\boldsymbol{\gamma}} = \begin{pmatrix} 2\epsilon u_x & \epsilon(u_y+v_x) & u_z+\epsilon^2 w_x \\ \epsilon(u_y+v_x) & 2\epsilon v_y & v_z+\epsilon^2 w_y \\ u_z+\epsilon^2 w_x & v_z+\epsilon^2 w_y & 2\epsilon w_z \end{pmatrix}. \tag{15}$$

The nondimensional boundary conditions at $z = 0$ can be written as:

$$u = 0, \;\; w = w_s(x, y, t), \;\; \text{at} \;\; z = 0, \tag{16a}$$

$$\theta_z = \epsilon^2 Pe(\theta - 1)w_s + b(\theta - \theta_s), \;\; \text{at} \;\; z = 0. \tag{16b}$$

where

$$w_s = [9Q_{s_0}Q_s(t)/16]\left[1-\left(\frac{x}{x_0}\right)^2\right]_+\left[1-\left(\frac{y}{y_0}\right)^2\right]_+, \tag{17}$$

where Q_{s_0} is a dimensionless parameter, $Q_{s_0} = Q_{s_0}^*/(x_0^* y_0^* \epsilon U)$ and $Q_{s_0}^*$ is a characteristic source flow rate, and the dimensionless vent width is $(x_0, y_0) = (x_0^*, y_0^*)/L^*$. The nondimensional boundary conditions at $z = h(x, y, t)$ are given by

$$h_t + uh_x + vh_y = w, \tag{18a}$$

$$p = \frac{\epsilon}{[1+\epsilon^2(h_x^2+h_y^2)]}\left(\tau_{zz} + \epsilon^2 h_x^2\tau_{xx} + \epsilon^2 h_y^2\tau_{yy} - 2\epsilon h_x\tau_{xz} - 2\epsilon h_y\tau_{yz} + 2\epsilon^2 h_x h_y\tau_{xy}\right), \tag{18b}$$

$$\tau_{xz}(1-\epsilon^2 h_x^2) + \epsilon h_x(\tau_{zz}-\tau_{xx}) - \epsilon h_y\tau_{xy} - \epsilon^2 h_x h_y\tau_{yz} = 0, \tag{18c}$$

$$\tau_{yz}(1-\epsilon^2 h_y^2) + \epsilon h_y(\tau_{zz}-\tau_{yy}) - \epsilon h_x\tau_{xy} - \epsilon^2 h_x h_y\tau_{xz} = 0, \tag{18d}$$

$$\theta_z = \epsilon^2 h_x\theta_x + \epsilon^2 h_y\theta_y - a\theta\sqrt{1+\epsilon^2 h_x^2+\epsilon^2 h_y^2}. \tag{18e}$$

The dimensionless parameters are: $S = \tan\beta/\epsilon$, is a measure of the downslope, $(0 \le S < \infty)$, the Reynold's number, $Re = U^*L^*/\mu_R^* = (g^* H^{*^3}/\mu_R^{*^2})\cos\theta$, compares inertial and viscous effects (assumed to be small, so inertial effects are neglected), the Péclet number, $Pe = (\rho^* c_p^* U^* L^*)/\kappa^*$, compares convective and diffusive heat transport, the heat transfer coefficients at the free surface and substrate, $b = b_s^* H^*/\kappa^*$ and $a = a_m^* H^*/\kappa^*$, respectively, $\alpha = \alpha^*(T_e^* - T_a^*)$, is the decay constant and μ_{min} is a minimum viscosity limit in the exponential viscosity model.

C. Lubrication approximation and evolution equations

Using the lubrication approximation, the leading order equations governing the flow are given in Appendix A. We can sequentially solve for the $O(1)$ quantities, using which the evolution equation for $h(x,y,t)$ can be derived. The details of the derivation are provided in Appendix A. The depth-averaged evolution equation for h is given by:

$$h_t + Q_x^{(x)} + Q_y^{(y)} = w_s. \tag{19}$$

Using the expressions for $Q^{(x)}$, $Q^{(y)}$ given in Eq. (A6), we can write the evolution equation for $h(x,y,t)$ as:

$$h_t = \nabla\cdot\left(\left[\int_0^h \frac{(h-z)^2}{\mu(\theta)}dz\right]\nabla h\right) - S\left(\int_0^h \frac{(h-z)^2}{\mu(\theta)}dz\right)_x + w_s, \tag{20}$$

where $w_s(x,y,t)$ is given by Eq. (17). We note that the lubrication approximation limits the leading order flow within the dome to be dominated by viscous shear with extensional (straining) flows relegated to $O(\epsilon^2)$ which are neglected here. For sufficiently large changes in viscosity a complicated mixture of shearing and extensional (straining) flows particularly in a thin diffusive skin near the free surface could generate additional viscous resistance, which could have a significant influence on the evolution and spreading characteristics. A "skin theory" developed by Balmforth, Craster, and Sassi [18] applies in this situation.

The flow is coupled with the temperature field via the viscosity relationship $\mu(\theta)$ given in Eq. (14). The nondimensionalised governing equation and boundary conditions for the temperature field are given by:

$$Pe_r\left[\theta_t + u\theta_x + v\theta_y + w\theta_z\right] = \epsilon^2\theta_{xx} + \epsilon^2\theta_{yy} + \theta_{zz}, \tag{21a}$$

$$\theta_z = Pe_r(\theta-1)w_s + b(\theta-\theta_s), \quad \text{at} \quad z=0, \tag{21b}$$

$$\theta_z = \epsilon^2 h_x\theta_x + \epsilon^2 h_y\theta_y - a\theta\sqrt{1+\epsilon^2h_x^2+\epsilon^2h_y^2}, \quad \text{at} \quad z=h(x,y,t), \tag{21c}$$

where the flow speeds, u,v and w are given by (A3a,A3b) and (A4), respectively. We consider the general case where the reduced Péclet number, $Pe_r = \epsilon^2 Pe = O(1)$, so that the heat convection terms on the left-hand-side of Eq. (21a) are of the same order as the vertical conduction term on the right-hand-side (third term on the right-hand-side of Eq. (21a)).

For future reference, we also consider the particular case of Eqs. (20,21) in the limit where the reduced Péclet number, $Pe_r = O(\epsilon^2)$, so that the Péclet number, $Pe = O(1)$, and $(a,b) = O(\epsilon^2)$. This is referred to as the conduction-dominated scenario. In this limit, the leading order θ is independent of z (vertically isothermal) and the integrals in Eq. (20) can be evaluated analytically. Using this, Eq. (20) can be reduced to Eq. (22a) given below for the evolution equation for the free surface $h(x,y,t)$. Moreover, the limit of small Péclet number allows the higher-order effects of diffusion in x and y at $O(\epsilon^2)$ to enter into the temperature equation, Eq. (21a), at the same order as convection, and that taking an integral in z then furnishes Eq. (22b) below for the temperature field $\theta(x,y,t)$. The evolution equations for relatively small Péclet number are given by (see derivation in Appendix B):

$$h_t = \frac{1}{3\mu(\theta)}\nabla\cdot(h^3\nabla h) - \frac{S}{3\mu(\theta)}(h^3)_x + w_s, \tag{22a}$$

$$\theta_t = -\frac{1}{h}\left[\mathbf{Q} - \frac{1}{Pe}\nabla h\right]\cdot\nabla\theta + \frac{1}{Pe}\nabla^2\theta - \frac{1}{hPe}[a\theta + b(\theta-\theta_s)] + \frac{w_s}{h}(1-\theta), \tag{22b}$$

where $\mathbf{Q}=(Q^{(x)},Q^{(y)})=\left(\frac{1}{3}\frac{h^3}{\mu(\theta)}(S-h_x), -\frac{1}{3}\frac{h^3}{\mu(\theta)}h_y\right)$.

Equation (22a) shows the contribution to the evolution of h from the fluxes due to the horizontal and vertical components of gravity (first and second term on the right, respectively). The evolution of the temperature, θ, given in Eq. (22b) shows the contribution to the heat transport due to: convection by the flow (first term on the right), diffusion or conduction (second term on the right), heat loss or cooling to the colder surrounding air and substrate and the gain in heat coming from the source (last 2 terms on the right, respectively).

Eqs. (20,22a), are the same as those derived in previous related studies[17,18], except for the inclusion of the horizontal component of gravity term via the downslope parameter S.

III. NUMERICAL SOLUTIONS

We seek numerical solutions of the evolution of the dome height, h, and the temperature field, θ, by varying the key parameters: the reduced Péclet number Pe_r (or the Péclet number Pe in the conduction-dominated scenario), the heat transfer coefficients, a,b, at the free surface and substrate, respectively, and the temperature-viscosity coupling constant, α, in the temperature-viscosity relationship. We do not restrict the choice of the values of the above parameters based on specific flow scenarios, but allow for a full range of realistic values to be explored in (Pe_r (or Pe), a,b,α) space.

We consider variations in the above parameters for $\epsilon = 0.1$, $S = 1$ (plane inclined at angle of approximately 6^o - a representative choice corresponding to the average slope of a typical terrain in real lava flows), and for constant volume or zero source flux ($Q_{s_0} = 0$) and constant flux. The inclination angle chosen above vis the parameter S is just representative; the qualitative features of the evolution and the instability are not influenced by this. We do not show results corresponding to $S = 0$ (horizontal plane). These have been investigated in the

works by Sansom *et al.*[15,16] and Balmforth *et al.*[17,18]; we will refer to this case when comparing with the spreading on an inclined plane.

While the precursor layer thickness does not affect the bulk flow, it influences the steepness of the liquid front at the dome's leading edge. We do not show any results varying δ (where $\delta = H_b^*/H^*$ is a dimensionless precursor layer thickness); in all the simulations shown below we fix the value of $\delta = 10^{-3}$ to represent the dynamics of a thin precursor layer.

A. y - independent evolution: The 1D time-dependent base state

We first investigate the evolution characteristics assuming that there is no variation in the y-direction transverse to the flow. Equation (20) for $h(x,t)$ is solved for $x \in [-L, L]$, where L is the length of the computational domain. For nonzero source flux, we assume the vent to be one-dimensional akin to a line source between $-x_0 \le x \le x_0$, and the vertical velocity through the vent is $w_s(x,t) = (9Q_{s_0}Q_s(t)/16)[1-(x/x_0)^2]_+$.

The two-dimensional evolution equation for the temperature, $\theta(x,z,t)$, Eq. (21a), is solved for $(x,z) \in [-L,L] \times [0, h(x,t)]$ with boundary conditions given by Eqs. (21b, 21c) at $z = 0, h(x,t)$, respectively, and $\theta_x = 0$ at $x = \pm L$. For computational convenience, it is useful to map the temperature field, $\theta(x,z,t)$, onto a rectangular domain using the change of variables $\bar{z} = z/h$. The transformed evolution equation for the temperature, $\theta(x,\bar{z},t)$ is solved for $(x,\bar{z}) \in [-L,L]\times[0,1]$. The transformed evolution equations for h and θ are given by Eqs. (C3$a-f$) shown in Appendix C. In what follows, we drop the bar in z with the implicit understanding that $z \in [0,1]$.

The initial conditions for h and θ are chosen as:

$$h(x,0) = (1-x^2)\mathcal{H}(1-x^2) + \delta,$$
$$\theta(x,0) = \mathcal{H}(1-x^2), \quad x \in [-L, L]. \tag{23}$$

$\mathcal{H}$ is the Heaviside function. The initial conditions represent a one-dimensional parabolic liquid dome at uniform temperature $\theta = 1$ (or $T^* = T_e^*$) between $-1 \le x \le 1$ connecting onto the precursor layer which is at temperature $\theta = 0$ (or $T^* = T_a^*$).

The boundary conditions are: $h \to \delta$ and $\theta_x \to 0$ as $x \to \pm\infty$. The length of the computational domain L is chosen sufficiently large so that the bulk of the fluid never reaches the edge of the domain for the times considered here. Otherwise, these boundary conditions would impact the flow.

The equations are solved numerically using the Method of Lines[21,22] on a uniform and fixed computational mesh in the spatial directions (x,z). The spatial derivatives are discretised using second-order centered finite difference schemes including a first-order upwind scheme for convection terms in the temperature equation, and the time derivative is kept continuous. We use the trapezoidal rule to approximate the integrals in Eqs. (A3,A4,20). The resulting system of differential-algebraic equations for the unknowns in h and θ at each grid point are solved in MATLAB (Release 2013a, The MathWorks Inc., Natick, Massachusetts, United States) using the stiff ODE solver *ode15i*.

Typical domain lengths in the x-direction varied between 10 units for simulations without a fluid source and 20 units for those including a fluid source. These were sufficiently long to capture the essential features of the spreading process as well as to satisfy the boundary conditions. The corresponding computational mesh sizes were $\Delta x = 10^{-2}$ in the x-direction and $\Delta z = 10^{-2} - 10^{-1}$ in the z-direction resulting in a system of $O(10^4 - 10^5)$ differential-algebraic equations (DAEs) required to be solved at each time step. For $Pe_r \gg 1$, the problem can have very narrow thermal boundary layers near $z = 0, h(x,t)$ of width $O(Pe_r^{-1/3})$. The smallest value of $\Delta z = 10^{-2}$ is sufficient to resolve these boundary layers for $Pe_r \le 10^4$. For $Pe_r > 10^4$, much smaller values of Δz are required which increases the number of DAEs at each time step, hence the computational effort. These results are not shown here as they are not different from the $Pe_r = 10^4$ results.

The time step was controlled within the solver to maintain the stability of the numerical solutions. The accuracy and convergence of the numerical scheme are formally checked for sample cases corresponding to a low, intermediate and high reduced Péclet number Pe_r. This is done as follows. At a specified time, t, we measure the error in the solution for h and θ using the max norm for decreasing mesh sizes, Δx, Δz. This is done systematically by (i) varying Δx, keeping Δz fixed, and (ii) varying Δz, keeping Δx fixed. Based on this, we can confirm that for the mesh sizes stated above the numerical solutions presented below are an accurate reflection of the spreading process.

We first consider the results for $S = 1$ and $Q_{s_0} = 0$ (constant volume drop). The other parameter values kept fixed are: $\alpha = 2$, $a = 0.02$ and $b = 0.03$. In Fig. 2($a-c$), ($d-f$) and ($g-i$), we show the contour plot for $\theta(x,z,t)$ at times $t = 1$ (a,d,g), $t = 14$ (b,e,h) and $t = 30$ (c,f,i) for varying $Pe_r = 10, 10^2, 10^4$. The temperature contours are superimposed on the corresponding free surface profiles, $h(x,t)$. We observe that, in general, the free surface profiles are non-symmetric about $x = 0$ and the dome slumps as it spreads with a steep front at its leading edge where it connects onto the precursor film. For large Pe_r (represented by $Pe_r = 10^4$), we observe from the contour plots shown in Fig. 2($g-i$) for $\theta(x,z,t)$ that the cooling is localised near the dome's leading edge forming a collar of cooler liquid there. The collar of cooler liquid is formed due to advection of the cooler liquid at the surface being deposited to the dome edge. The bulk liquid within the dome is insulated at a higher temperature $\theta \approx 1$ (or $T^* = T_e^*$, the initial temperature). This results in a much lower overall viscosity, and consequently faster spreading compared to lower values of Pe_r. On the other

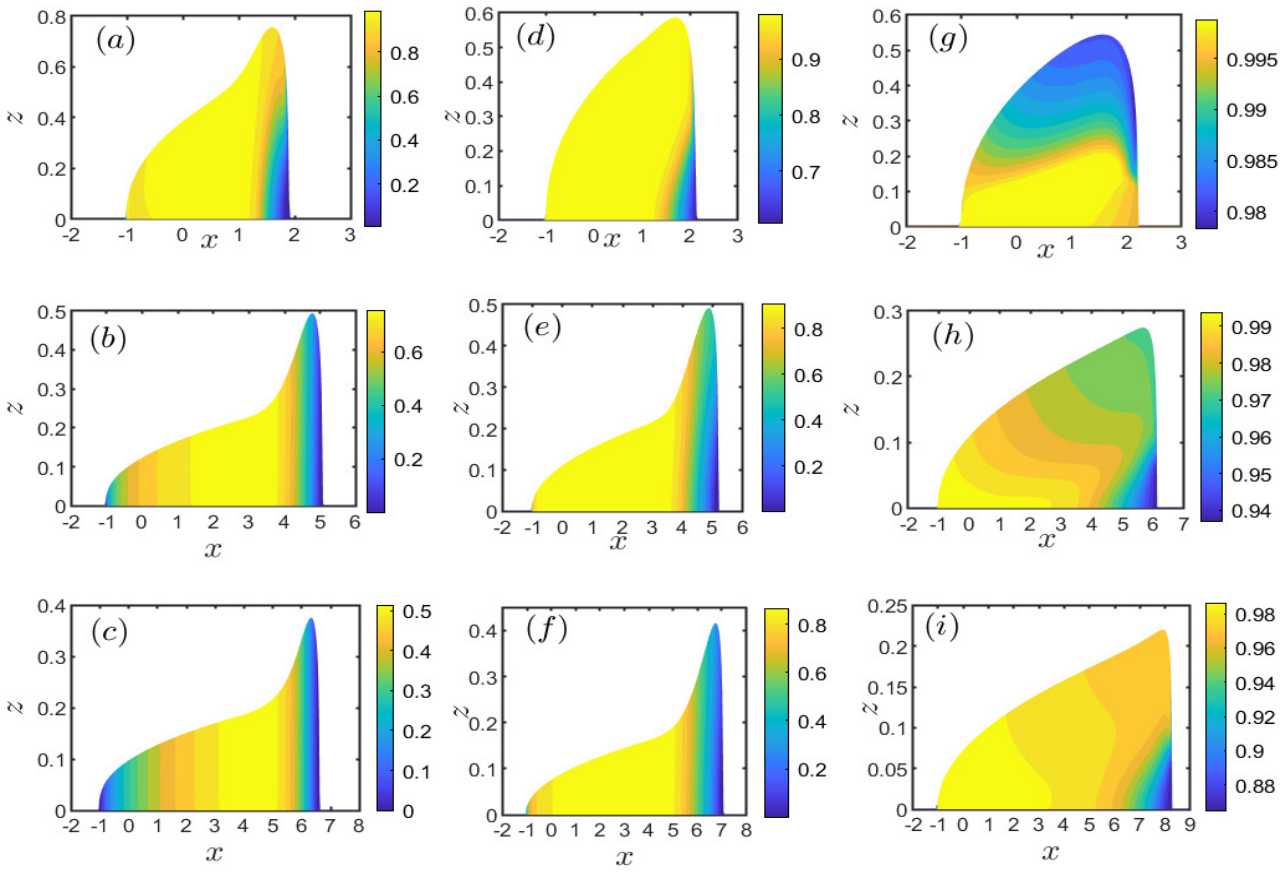

Figure 2: The contour plot for (a) $\theta(x,z,t=1)$, (b) $\theta(x,z,t=14)$ and (c) $\theta(x,z,t=30)$ for $Pe_r=10$, (d) $\theta(x,z,t=1)$, (e) $\theta(x,z,t=14)$ and (f) $\theta(x,z,t=30)$ for $Pe_r=10^2$, and (g) $\theta(x,z,t=1)$, (h) $\theta(x,z,t=14)$ and (i) $\theta(x,z,t=30)$ for $Pe_r=10^4$. The other parameter values kept fixed are: $\alpha=2$, $Q_{s_0}=0$, $\theta_s=0$, $a=0.02$ and $b=0.03$.

hand, for small Pe_r (results not shown here), the cooling is uniform over the entire domain resulting in the temperature quickly dropping uniformly to its equilibrium value, $\theta=0$ (or $T^*=T_a^*$, the ambient temperature). Once this is achieved and the liquid viscosity is almost everywhere $\mu(\theta)=1$, the free surface evolution of $h(x,t)$ is similar to that of isothermal spreading at that viscosity. As the overall viscosity is higher than that at large vales of Pe_r, the spreading is comparatively slower. Figure 2$(a-c,d-f)$ capture the temperature variations for intermediate values of Pe_r represented by $Pe_r=10,10^2$, respectively. The cooling is less uniform in the flow direction compared to small and large Pe_r. There is loss of a large amount heat and consequently more pronounced cooling near the leading edge of the advancing front and the trailing edge of the dome where h is small, compared to elsewhere. This is due to the rate of heat loss per unit thickness being inversely proportional to h. The temperature within the bulk liquid in the dome remains almost at uniform and higher temperature. The temperature variations are almost uniform along any vertical cross-section of the dome's thickness. We observe the formation of a characteristic elevated fluid ridge developing near the dome's leading edge. The temperature behind the leading edge is much higher than that ahead; the increase in mobility due to the reduced liquid viscosity results in the hotter liquid piling-up over the relatively colder liquid ahead of it resulting in the development of the elevated ridge in the free surface shape near the leading edge. This non-uniformity in cooling is absent for small Pe_r and not sufficiently strong at large Pe_r (due to the localised nature of the cooling close to the dome's leading edge), and hence precludes any piling-up of hotter liquid at the leading edge. Therefore, we do not observe the development of the fluid ridge for these cases.

Having established the existence of the fluid ridge, we further explore and characterize the evolution of $h(x,t)$ for varying Pe_r in Fig. 3$(a-f)$ making comparisons

with isothermal spreading. The other parameter values are fixed at $\alpha = 2$, $a = 0.02$ and $b = 0.03$. The dashed curves in Fig. 3(a,d) show the evolution of $h(x,t)$ for $t = 0-30$ with $\mu = 1$ (or $\theta = 0$ everywhere corresponding to a dome with liquid at the ambient temperature, T_a^*) and $\mu_{min} = 10^{-3}$ (or $\theta = 1$ corresponding to a dome with liquid at a hotter temperature, T_e^*), respectively. Both these cases are isothermal with differing liquid viscosities. The solid curves in Fig. 3(a,b,c,d) show the evolution of $h(x,t)$ for $t = 0-30$ for $Pe_r = 10^{-1}, 10, 10^2, 10^4$, respectively. For small Pe_r (represented by $Pe_r = 10^{-1}$ - solid curves in Fig. 3(a)), the liquid viscosity is almost everywhere $\mu(\theta) = 1$, the evolution of $h(x,t)$ is similar to that of isothermal spreading at that viscosity (dashed curves in Fig. 3(a)). This is consistent with the long-time self-similar solution $h = \sqrt{\mu(\theta)x/(St)}$ for isothermal spreading[23,24]. For much larger Pe_r (represented by $Pe_r = 10^4$ - solid curves in Fig. 3(d)), the liquid viscosity is almost everywhere $\mu(\theta) = \mu_{min}$. This results in a much lower overall viscosity, and consequently faster spreading compared to lower values of Pe_r. The evolution of $h(x,t)$ is almost indistinguishable from that of isothermal spreading with $\mu(\theta) = \mu_{min}$ (dashed curves in Fig. 3(d)) even at early time. For intermediate Pe_r (represented by $Pe_r = 10, 10^2$ - solid curves in Fig. 3(b,c)), we clearly observe the development of the fluid ridge at the leading edge of the dome which gradually subsides in time.

Figures 3(e,f) track the evolution of the location of the dome's front, $x_f(t)$, and the corresponding thickness, $h_f = h(x_f,t)$, respectively, as a function of t for Pe_r between $10^{-1} \le Pe_r \le 10^4$. The location of x_f is assumed to be where the dome attains its maximum thickness h_f near the leading edge. We observe that x_f is always bounded by the two isothermal curves corresponding to $\mu(\theta) = 1, \mu_{min}$, respectively (dashed curves in Fig. 3(e)). The spreading rates for small and large Pe_r tend to these limiting rates. We observe the spreading rate for smaller Pe_r tends to that corresponding to $\mu = 1$ much slower than for larger Pe_r, which is indistinguishable from the spreading rate corresponding to $\mu = \mu_{min}$ from very early time (also see Fig. 3(a,d)). This is due to the delay in the dome uniformly cooling from $\theta = 1$ to $\theta = 0$ for small Pe_r whereas for larger Pe_r, the bulk liquid is always insulated at $\theta = 1$.

For constant volume and isothermal spreading, the long-time spreading rate is $x_{f,iso}(t) = [9SV^2/(4\mu(\theta))]^{1/3}t^{1/3}$[23,24], where V is the dome's volume. Hence, $[9SV^2/4]^{1/3}t^{1/3} \le x_{f,iso}(t) \le [9SV^2/(4\mu_{min})]^{1/3}t^{1/3}$ for $0 \le \theta \le 1$. Similarly, $h_{f,iso}(t)$ is bounded by the two limiting isothermal curves represented by the dashed curves in Fig. 3(f). The long-time behaviour is $h_{f,iso}(t) = \sqrt{\mu(\theta)x_{f,iso}/(St)} = [3V\mu(\theta)/(2S)]^{1/3}t^{-1/3}$[23,24], hence $[3V\mu_{min}/(2S)]^{1/3}t^{-1/3} \le h_{f,iso}(t) \le [3V/(2S)]^{1/3}t^{-1/3}$ for $0 \le \theta \le 1$. We also note that for isothermal spreading, the evolution for h does not exhibit a fluid ridge but will monotonically increase to the maximum height $h_{f,iso}(t)$ (see dashed curves in Fig. 3(a,d)). We observe from Fig. 3(f) that for $Pe_r = 10^{-1}$, $h_f(t)$ is almost parallel to the limiting curves indicating that the spreading behaviour is close to isothermal with no fluid ridge. For $Pe_r = 10, 10^2$, a fluid ridge is guaranteed to exist with h_f overshooting $h_{f,iso}$ at $\theta = 0$. For $Pe_r = 10^4$, the spreading behaviour is again close to isothermal with no fluid ridge.

We conclude this section by considering the effects of an influx of liquid from a source or vent with $Q_{s_0} = 5$ (representative non-zero source flux). Figure 4 shows the influence of the source flux with $Pe_r = 10^2$, $\alpha = 2$, $a = b = 0.02$. The free surface profiles show a noticeable growing ridge over the majority of the dome (Fig. 4(a)). The temperature profiles show maximum cooling near the flow front causing build up of very viscous cold fluid there. The hot interior fluid piles-up over this cooler region and develops a fluid ridge. The mechanism is similar to the case of $Q_{s_0} = 0$, (zero source flux) except that the constant flux through the vent increases the volume of hot fluid piling-up into the fluid ridge.

IV. MAPPING THE FLUID RIDGE IN PARAMETER SPACE FOR $Pe_r \ll 1$

In this section, we conduct a parameter survey in $(Pe, a = b, \alpha)$ space shown in Fig. 5 to investigate the existence of free surface shapes, $h(x,t)$, with and without a fluid ridge near the leading edge. We use the conduction-dominated scenario given by Eq. (22) valid in the limit $Pe_r = \epsilon^2 Pe \ll 1$ ($Pe = O(1)$) to plot the curves in Fig. 5. This is less computationally intensive compared to the $Pe_r = O(1)$ case. For a typical value of $\epsilon = 0.1$, the range of values $0 \le Pe_r \le 10^2$ (or $0 \le Pe \le 10^4$) have been used in the above calculations. While this is strictly outside the range of validity of the conduction-dominated asymptotic analysis, nevertheless there is evidence from our $Pe_r = O(1)$ calculations that this still holds, for example, see Fig. 2$(a-f)$ where $\theta(x,z,t)$ is almost everywhere independent of z.

We use a geometric criterion to quantify the elevation of the ridge (see Appendix D for details). This is based on the change in the local angle of elevation given by $\tan^{-1}(h_x|_{\max}) - \tan^{-1}(h_x|_{\min})$ should exceed a prescribed threshold value during the evolution. If this is the case, then the ridge is classified to be elevated. We use the threshold criterion that the local angle of elevation described above should exceed 10^o over the prescribed period of time that the simulations are run in order to plot the parameter survey in Fig. 5. The black, green and red circles separate the no ridge regions from the ridge regions for $\alpha = 2, 4, 6$, respectively.

Figure 5 shows that the region where ridges are observed expands as α increases. We also note here that the height of the fluid ridge gets bigger as α increases (not shown). This is due to the liquid viscosity contrast

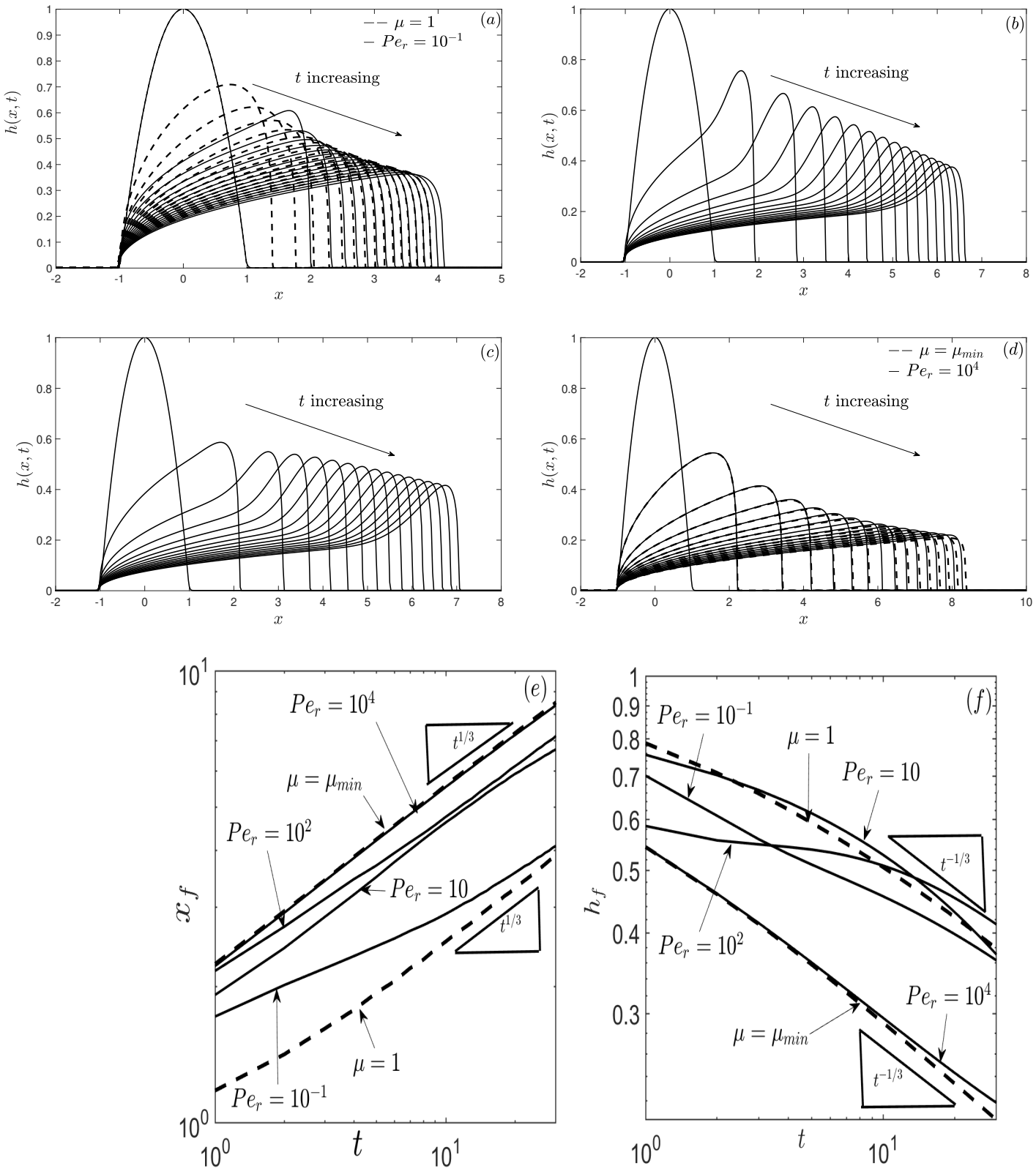

Figure 3: The evolution of $h(x,t)$ for t varying between $t = 0 - 30$ corresponding to (a) $Pe_r = 10^{-1}$ (solid curves) and $\mu = 1$ (dashed curves; isothermal case with $\theta = 0$), (b) $Pe_r = 10$, (c) $Pe_r = 10^2$, (d) $Pe_r = 10^4$ (solid curves) and $\mu = \mu_{min} = 10^{-3}$ (dashed curves; isothermal case with $\theta = 1$). The evolution of (e) the leading edge of the dome, x_f, and (f) the maximum in h, $h_f = h(x_f, t)$, as a function of time, t, for various reduced Péclet number, Pe_r. The parameter values are: $S = 1$ (plane inclined at 6^o), $\alpha = 2$, $Q_{s_0} = 0$, $\theta_s = 0$, $a = 0.02$ and $b = 0.03$.

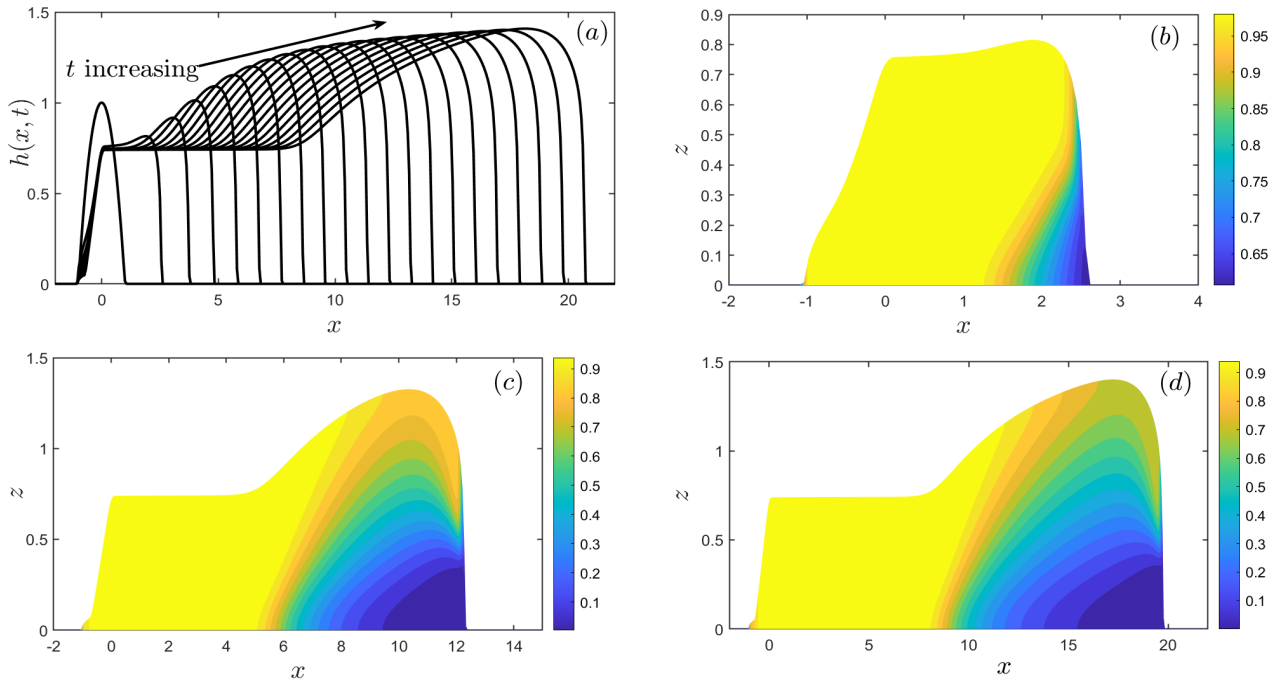

Figure 4: The evolution of (a) $h(x,t)$ for t varying between $t = 0 - 20$ and the contour plot for (b) $\theta(x, z, t = 1)$, (c) $\theta(x, z, t = 12)$, and (d) $\theta(x, z, t = 20)$, with $S = 1$, $Pe_r = 10^2$, $\alpha = 2$, $Q_{s_0} = 5$, $\theta_s = 0$, $a = b = 0.02$.

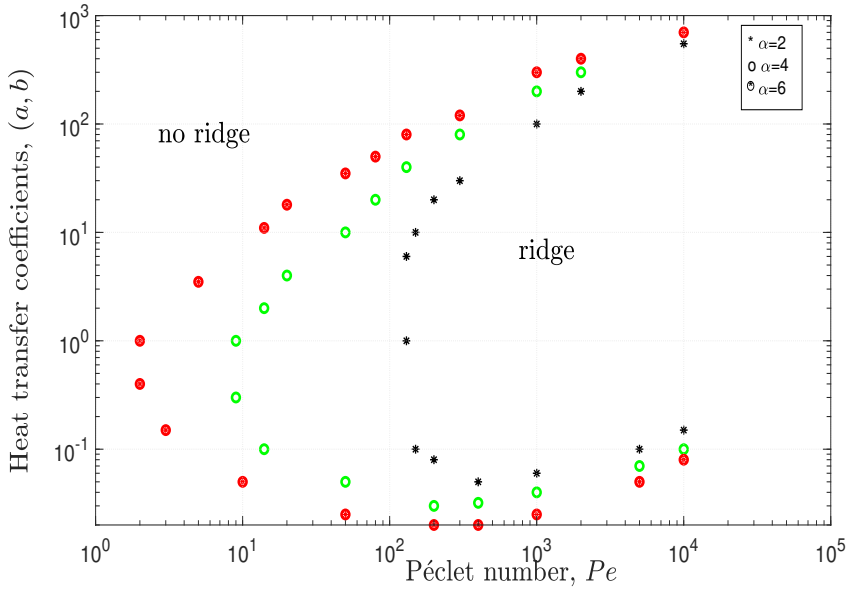

Figure 5: Parameter survey in $(Pe, a = b, \alpha)$ space for the conduction-dominated case to show existence of free surface shapes, $h(x,t)$ with and without a fluid ridge near the leading edge. The black, green and red circles separate the no ridge regions from the ridge regions for $\alpha = 2, 4, 6$, respectively. The parameter values are: $S = 1$ (inclination angle approximately 6^o) and $\epsilon = 0.1$.

between the hotter bulk liquid behind the front and the colder liquid at the front being even more enhanced for larger values of α. We observe that no ridges exist for very low and high values of a, b; at these values cooling of the liquid in the dome is either uniformly negligible or rapid resulting in the mechanism of ridge formation being suppressed.

We also note that for the $S = 0$ (horizontal plane) case (not shown), there are no solutions exhibiting a ridge in $(Pe, a = b, \alpha)$ space - the evolution of h follows either a symmetrically flattening dome profile or a pancake-shaped profile[15–18]. Therefore, the inclination of the plane is necessary to enhance the liquid mobility resulting in the formation of the ridge at the dome's leading edge. Increasing the inclination angle is observed to enhance the elevation of the ridge.

V. STABILITY TO TRANSVERSE PERTURBATIONS FOR $Pe_r \ll 1$

In this section, we examine the transverse stability of the conduction-dominated (or vertically isothermal) scenario given by Eq. (22) to small-amplitude transverse perturbations superimposed on a base state flow and temperature field. We do this using both a transient linear stability analysis (§V A) and nonlinear stability analysis via two-dimensional numerical simulations (§V B). The base state flow and temperature are represented by the $y-$ independent numerical solutions that have been computed in §III A in the limit $Pe_r = \epsilon^2 Pe \ll 1$ ($Pe = O(1)$).

We focus on investigating the linear and nonlinear stability of the elevated ridge solution. In order to do this, we choose an initial base state for h that has already formed an elevated ridge. For the parameter values considered below, the earliest time when the $y-$ independent solution for h forms an elevated ridge is $t = 2$. We use this and the corresponding solution for θ to represent the initial base states $(h, \theta)_0(x, t = 0)$ for the stability study in §V A and V B. We do the same for investigating the stability of the case without an elevated ridge. Based on the above considerations, the starting time for the stability calculations shown below is $t = 0$.

For the parameters, we choose $S = 1$ and $w_s(x, t) = 0$ and focus on varying Pe, a, b and α. We vary these based on the parameter survey conducted in $(Pe, a = b, \alpha)$ space (Fig. 5) for representative base states displaying a fluid ridge or not in their evolution.

A. Linear stability analysis

We impose a perturbation on the base states obtained from the y-independent solutions, $(h, \theta)_0(x, t)$ (say), with small disturbances, $(h, \theta)_1(x, t)$, of prescribed transverse wavenumber k (of the form e^{iky}). Substituting into (22), we obtain the evolution equations for $(h, \theta)_1$:

$$h_{1_t} + \frac{1}{3}\left[\frac{3h_0^2 h_1 (S - h_{0_x}) - h_0^3 h_{1_x} - \mu_1(\theta_0, \theta_1)\frac{h_0^3 (S - h_{0_x})}{\mu_0(\theta_0)}}{\mu_0(\theta_0)}\right]_x + \frac{1}{3}k^2 \frac{h_0^3 h_1}{\mu_0(\theta_0)} = 0, \tag{24a}$$

$$\theta_{1_t} + \frac{h_1}{h_0}\theta_{0_t} + \frac{1}{3}\frac{h_0^2}{\mu_0(\theta_0)}(S - h_{0_x})\theta_{1_x} + \frac{\theta_{0_x}}{3}\left[\frac{3h_0 h_1}{\mu_0(\theta_0)}(S - h_{0_x}) - \frac{h_0^2 h_{1_x}}{\mu_0(\theta_0)} - \frac{h_0^2 \mu_1(\theta_0, \theta_1)}{\mu_0^2(\theta_0)}(S - h_{0_x})\right] = \frac{1}{h_0 Pe}\left[h_0 \theta_{1_x} + h_1 \theta_{0_x}\right]_x - \frac{1}{h_0 Pe}k^2 h_0 \theta_1 - \frac{1}{h_0 Pe}\left[a + b + w_s\right]\theta_1, \tag{24b}$$

$$\mu_0(\theta_0) = (1 - \mu_{min})e^{-\alpha\theta_0} + \mu_{min},$$
$$\mu_1(\theta_0, \theta_1) = -(1 - \mu_{min})\alpha\theta_1 e^{-\alpha\theta_0}. \tag{24c}$$

These are subject to the boundary conditions $(h, \theta)_1 \to 0$ and all their derivatives decay to zero as $x \to \pm\infty$.

The time-dependence of the base states (h_0, θ_0) prevents the application of normal mode analysis to determine the dispersion relationship and necessary and sufficient conditions for the linear instability. One can 'freeze' the base states at a given time and assume exponential growth or decay in $(h, \theta)_1 = (\phi_1, \phi_2)e^{\lambda t}$, where (ϕ_1, ϕ_2) are the eigenfunctions corresponding to a growth rate λ. Substituting this in Eq. (24) gives an eigenvalue problem, solving which provides the dispersion relation for the instantaneous growth rate $\lambda = \lambda(k)$. One can then compute the dispersion relation for base states at different snapshots in time to determine the time variation of the growth rate as the base state evolves.

An alternative method, which we follow here, is to solve Eq. (24) as an initial value problem with prescribed initial conditions for the base states and perturbations. One can then measure the transient amplification of the perturbation and the corresponding growth rate relative to the evolving base states[25].

The initial base states $(h, \theta)_0(x, t)$ are chosen as mentioned at the beginning of this section. The corresponding initial conditions for the perturbations are chosen as: $(h_1, \theta_1) = A_0 \exp(-B_0(x - x_f)^2)$, where A_0, B_0 are the amplitude and width of the perturbation, respectively. The perturbations are imposed around the fluid ridge region at $x = x_f$ where we anticipate maximum amplification[16–19,26].

Eq. (24) coupled with the $y-$ independent form of Eq. (22) are solved numerically using the method of lines and ode15s in Matlab. The typical domain size was 20 units and the computational mesh size was $O(10^{-3})$; the amplitude and width of the perturbations $A_0 = 10^{-3}, B_0 = 10^2$, respectively. We investigate the transverse stability of two representative base states corresponding to $(Pe, a = b, \alpha)$ equal to: (i) $(10^2, 0.1, 2)$ (no ridge), and (ii) $(10^4, 10, 2)$ (ridge).

Figure 6(a,b) show a typical evolution of the base states (h_0,θ_0), respectively, and the superimposed perturbations (h $(\times 10^{-4})$, θ_1 $(\times 10^{-3})$), for $t=0-500$ in 50 time units. The parameter values are, $(Pe, a=b, \alpha, k) = (10^4, 10, 2, 3)$. We observe peaks in both (h_1,θ_1) in the vicinity of the leading edge of the dome - the peaks in h_1 are much steeper than those in θ_1. (h_1,θ_1) amplify in time suggesting that (h_0,θ_0) are linearly unstable for the parameter set considered. At much later times, (h_1,θ_1) become smaller as (h_0,θ_0) flatten out. Figure 6(c,d) show a close-up view of $(h_{0,1},\theta_{0,1})$ near the leading edge of the dome at $t=50$ for varying wavenumbers $k=1,3,10$. The peaks in (h_1,θ_1) coincide with the steep gradient in (h_0,θ_0), respectively. The peaks in h_1 are sharper than θ_1 due to the steeper gradient in h_0 compared to θ_0 in the vicinity of the flow front. For small values of k, we observe that $(h_1,\theta_1) \propto -(h_{0_x},\theta_{0_x})$ (see $k=1$ in Fig. 6(c,d)); $h_1<0$ between the peak and the back edge of the ridge, where $h_{0_x}>0$; $(h_1,\theta_1)>0$ at the leading edge of the dome, where $(h_{0_x},\theta_{0_x})<0$. As k increases, the magnitude of the peak in (h_1,θ_1) and the local minimum in h_1 at the back edge of the ridge increase with k ($k=3,10$ in Fig. 6(c,d) - note the difference in scaling with k shown). Moreover, we also observe that as k increases the width of the region where $h_1<0$ decreases with k (see $k=3,10$ in Fig. 6(c,d) between the peak and the back edge of the ridge in h_0).

Necessary condition for linear instability

The results in Fig. 6 demonstrate that the linear instability is localized around the leading edge x_f. Based on this, we define a local scaled variable $\xi = [x-x_f(t)]SPe^{1/3}$. We also define the scaled variables $h_{0,1}(x,t) = H_{0,1}(\xi,\tau)Pe^{-1/3}$, $\theta_{0,1}(x,t)=\theta_{0,1}(\xi,\tau)$, $t=(Pe^{1/3}/S^2)\tau$ and $k=SPe^{1/3}\hat{k}$. Substituting in Eq. (24a) gives:

$$H_{1_\tau} - \hat{x}_{f_\tau} H_{1_\xi} + \frac{1}{3}\left[\frac{3H_0^2H_1(1-H_{0_x}) - H_0^3H_{1_x} - \mu_1(\theta_0,\theta_1)\frac{H_0^3(1-H_{0_x})}{\mu_0(\theta_0)}}{\mu_0(\theta_0)}\right]_x + \frac{1}{3}\hat{k}^2\frac{H_0^3H_1}{\mu_0(\theta_0)} = 0, \tag{25}$$

where $\hat{x}_{f_\tau} = x_{f_\tau}SPe^{1/3}$. Integrating Eq. (25) between $\xi=\pm\infty$, and assuming that $(H,\theta)_1$ and all their derivatives decay to zero as as $\xi\to\pm\infty$, gives:

$$\frac{d}{dt}\int_{-\infty}^{\infty} H_1\, d\xi = -\frac{1}{3}\hat{k}^2\int_{-\infty}^{\infty}\frac{H_0^3H_1}{\mu_0(\theta_0)}\, d\xi. \tag{26}$$

For the time derivative of the integral to be positive (characterising a growing volume), a criterion for H_1 to be linearly unstable is then given by $\int_{-\infty}^{\infty}\frac{H_0^3H_1}{\mu_0(\theta_0)}\,dx<0$ provided $\int_{-\infty}^{\infty}H_1\,dx>0$ or $\int_{-\infty}^{\infty}\frac{H_0^3H_1}{\mu_0(\theta_0)}\,dx>0$ provided $\int_{-\infty}^{\infty}H_1\,dx<0$. Figure 7$(a)$ plots the unscaled volume integral $\int_{-\infty}^{\infty}h_1\,dx\left[=\frac{1}{SPe^{2/3}}\int_{-\infty}^{\infty}H_1\,d\xi\right]$ as a function of time t for varying wavenumbers $k=1,3,10,20$. For $k=1,3,10$, this integral is positive for the range of times shown. In fact, this also applies for $k\le 15$ (result not shown here). This is due to the contribution from $h_1>0$ at the dome's leading edge dominating the $h_1<0$ contribution between the peak and the back edge of the ridge. At early times, the integral increases with k; at later times the integral decreases as k increases. This integral can also become negative for the range of times shown (see $k=20$ in Fig. 7(a)). We note that the transition actually occurs around $k=15$ (result not shown here). For these values of k, h_1 changes sign with $h_1<0$ at the dome's leading edge dominating the $h_1>0$ contribution between the peak and the back edge of the ridge; the other characteristics of h_1 are similar to Fig. 6(c). The magnitude of this integral decreases as k increases. Figure 7(b) plots $-\frac{1}{3}k^2\int_{-\infty}^{\infty}\frac{h_0^3h_1}{\mu_0(\theta_0)}\,dx\left[=-\frac{S}{3Pe}\hat{k}^2\int_{-\infty}^{\infty}\frac{H_0^3H_1}{\mu_0(\theta_0)}\,d\xi\right]$ as a function of time for varying wavenumbers $k=1,3,10,20$. The linear instability criterion is satisfied at early times for the range of wavenumbers shown. For $k=1,3,10$, the dominant contribution to the integral is from the region between the peak and the back edge of the ridge where $\frac{h_0^3h_1}{\mu_0(\theta_0)}<0$. In fact, this also applies for $k\le 15$ (result not shown here). Here $h_0\sim h_f$ and $\mu_0(\theta_0)\sim\mu_{min}$ ensures that the contribution from $h_1<0$ dominates the $h_1>0$ contribution at the leading edge of the dome where $h_0\sim\delta$ and $\mu_0(\theta_0)\sim 1$. This physically translates to the increased mobility of the hotter liquid in the fluid ridge region compared to that in the colder region at the leading edge of the dome. Moreover, the severity of the linear instability increases with k at early times since this contribution increases with k (note that the magnitude of h_1 increases with k eventhough the width of this region decreases; see Fig. 6(c)). However, at later times, the linear instability gradually subsides as $\frac{h_0^3h_1}{\mu_0(\theta_0)}>0$ dominates the contribution to the integral at these times. The decay is quicker as k increases. For $k>20$, the dominant contribution to the integral at early times is again from the region between the peak and the back edge of the ridge where $\frac{h_0^3h_1}{\mu_0(\theta_0)}>0$, so $-\frac{1}{3}k^2\int_{-\infty}^{\infty}\frac{h_0^3h_1}{\mu_0(\theta_0)}\,dx<0$ (Fig. 7(b)). This also applies for $k\ge 15$ (result not shown here). Hence, the linear instability criterion still holds provided $\int_{-\infty}^{\infty}h_1\,dx<0$ (see $k=20$ in Fig. 7(a)). At later times, $\frac{h_0^3h_1}{\mu_0(\theta_0)}<0$ dominates the contribution to the

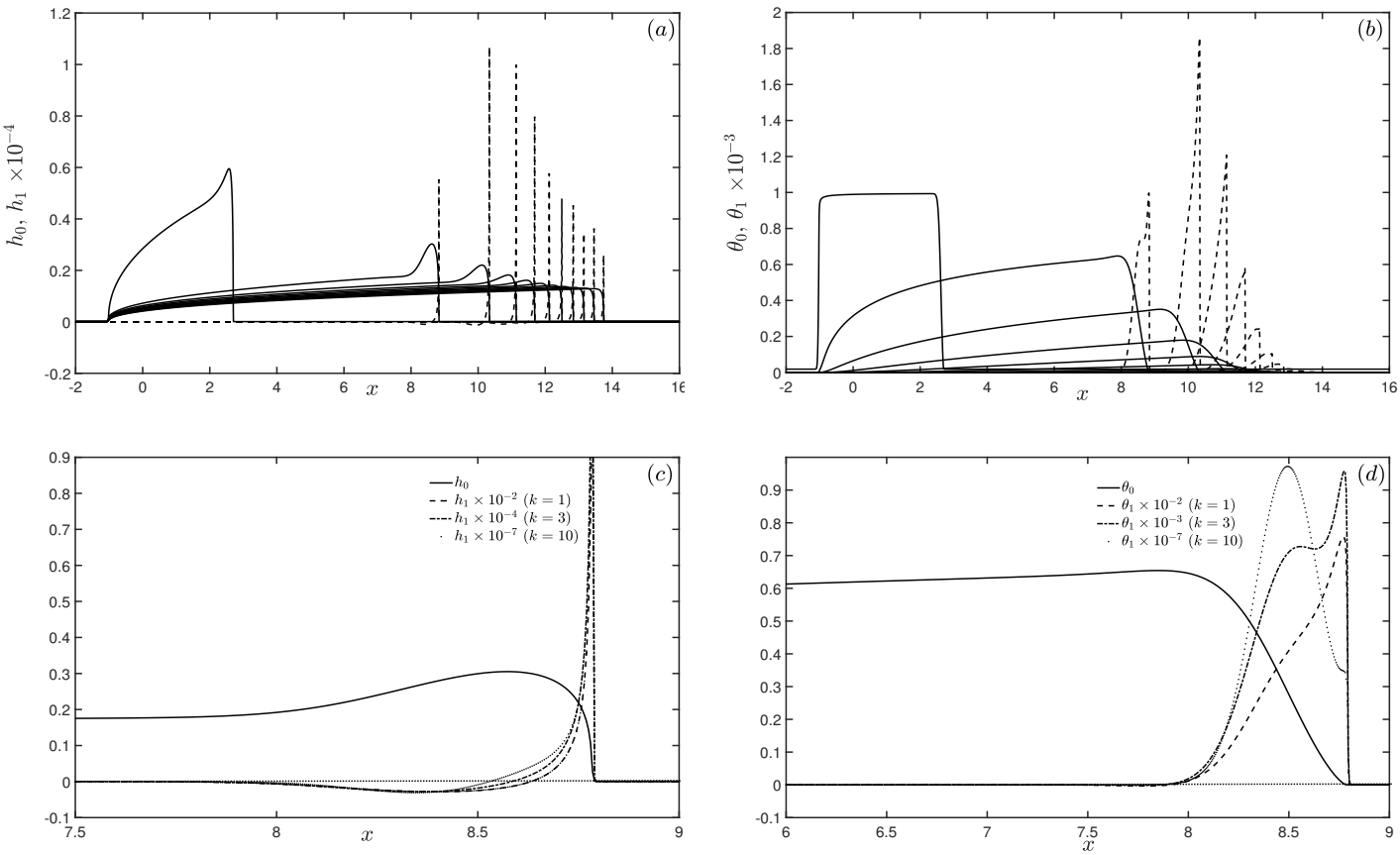

Figure 6: The evolution of (a) h_0 (solid) and h_1 $(\times 10^{-4})$ (dashed), and (b) θ_0 (solid) and θ_1 $(\times 10^{-3})$ (dashed) for $k = 3$ and $t = 0 - 500$ in 50 time units. (c) h_0, h_1 and (d) θ_0, θ_1 at $t = 50$ for $k = 1, 3, 10$. The parameter values are: $(Pe, a = b, \alpha) = (10^4, 10, 2)$.

integral and the linear instability gradually subsides. For small k, we can determine a necessary condition for instability based on the observation that $(h, \theta)_1 \propto -(h_0, \theta_0)_x$. $k = 1$ in Fig. 6(c) shows that $h_1 < 0$ in the region where h_0 displays a fluid ridge. Hence, a necessary condition for the base state h_0 to be linearly unstable is that it must exhibit a fluid ridge in the vicinity of the front. However, the fluid ridge is not sufficient for linear instability as observed at much later times when the fluid ridge in h_0 gradually subsides, the $h_1 > 0$ contribution starts dominating reducing the growth rate and eventually h_1 decays to zero. We also show a case corresponding to a lower Péclet number where the base state h_0 develops a weak ridge during the evolution. We classify this case as not displaying a ridged profile because the local elevation angle is lower than the threshold angle for the range of times considered. Figures 7(c, d) plot the unscaled volume integral $\int_{-\infty}^{\infty} h_1\ dx \left[= \dfrac{1}{SPe^{2/3}} \int_{-\infty}^{\infty} H_1\ d\xi\right]$ and $-\dfrac{1}{3}k^2 \int_{-\infty}^{\infty} \dfrac{h_0^3 h_1}{\mu_0(\theta_0)}\ dx \left[= -\dfrac{S}{3Pe}\hat{k}^2 \int_{-\infty}^{\infty} \dfrac{H_0^3 H_1}{\mu_0(\theta_0)}\ d\xi\right]$ as a function of time for varying wavenumbers $k = 1, 2, 3$ and $(Pe, a = b, \alpha) = (10^2, 0.1, 2)$. The first integral decreases in time from an initial volume of 1.8×10^{-4} with the rate of decrease increasing with k. For $k = 1$, there is a slight increase in volume around $t = 10$, and the volume decreases very slowly thereafter. The second integral is negative for $k = 2, 3$ suggesting that the $h_1 > 0$ contribution dominates near the leading edge, and the evolution is linearly stable. The contribution from $h_1 < 0$, although it still exits due to the weak ridge, is less dominant. For $k = 1$, the second integral becomes slightly positive around $t = 10$ when the base state starts developing a weak ridge, and the contribution from $h_1 < 0$ starts to dominate. This weak linear instability is not sustained and the integral becomes negative as time progresses due to a combination of further weakening of the ridge and $h_1 > 0$ contribution beginning to dominate. Hence, the evolution for this set of parameter values shows a weak linear instability gradually weakening in time for $k = 1$ and is linearly stable for all $k > 1$.

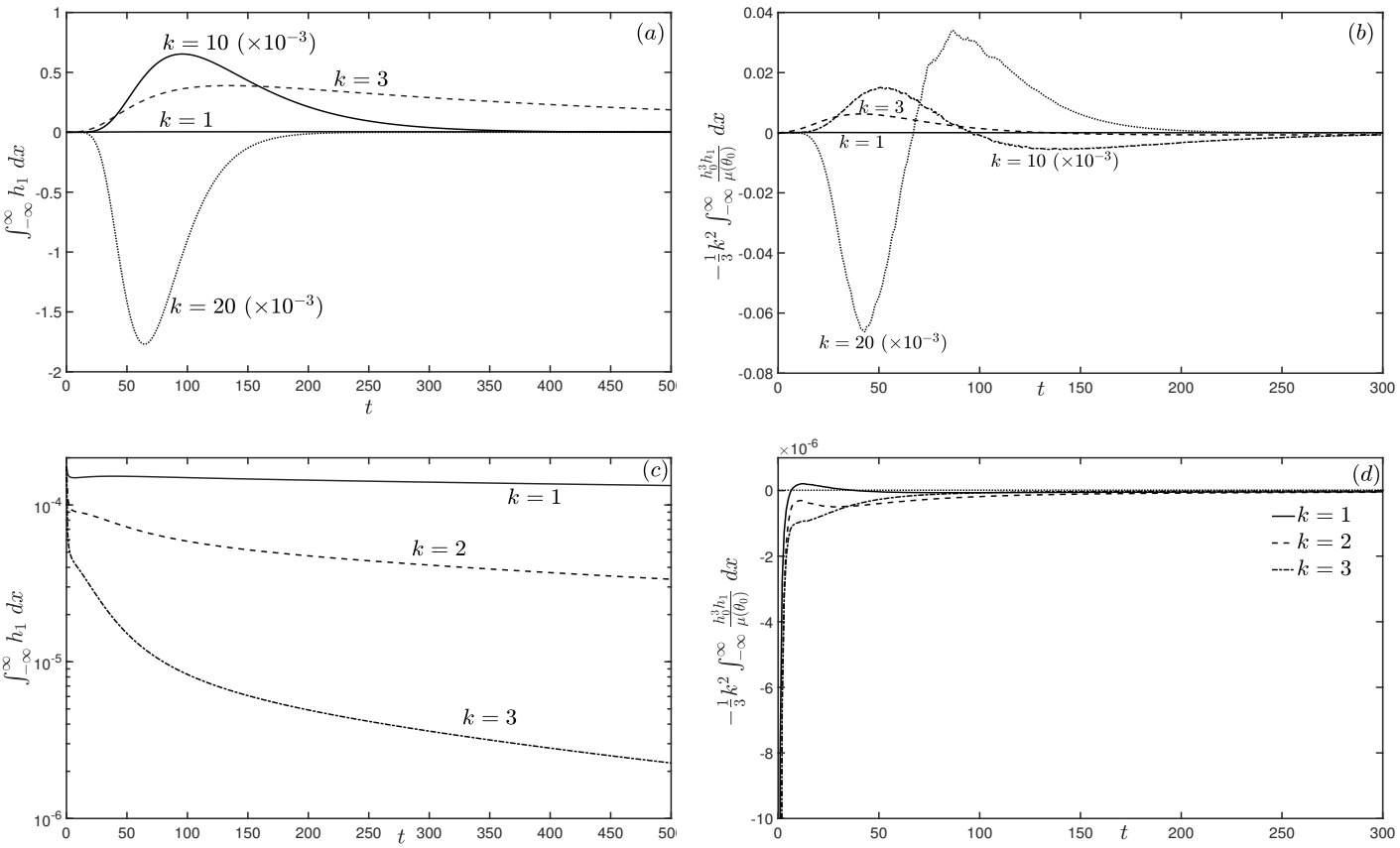

Figure 7: $(a)\ \int_{-\infty}^{\infty} h_1\ dx \left[= \frac{1}{SPe^{2/3}} \int_{-\infty}^{\infty} H_1\ d\xi\right]$, and $(b)\ -\frac{1}{3}k^2 \int_{-\infty}^{\infty} \frac{h_0^3 h_1}{\mu_0(\theta_0)}\ dx \left[= -\frac{S}{3Pe}\hat{k}^2 \int_{-\infty}^{\infty} \frac{H_0^3 H_1}{\mu_0(\theta_0)}\ d\xi\right]$ for $t = 0 - 500$ and $k = 1, 3, 10, 20$. The parameter values are: $(Pe, a = b, \alpha) = (10^4, 10, 2)$. $(c)\ \int_{-\infty}^{\infty} h_1\ dx$, and (d) $-\frac{1}{3}k^2 \int_{-\infty}^{\infty} \frac{h_0^3 h_1}{\mu_0(\theta_0)}\ dx$ for $t = 0 - 300$ and $k = 1, 2, 3$ for the parameter values $(Pe, a = b, \alpha) = (10^2, 0.1, 2)$.

Amplification of linear instability

To further strengthen the above assertions, we now consider the amplification and growth rates of the perturbations as a function of the wavenumber for the representative parameter values mentioned above. Based on the above considerations, the amplification and corresponding growth rate of the perturbations are measured as follows[25]:

$$A_h(t) = \left| \frac{E_{h_1}(t)/E_{h_0}(t)}{E_{h_1}(t=0)/E_{h_0}(0)} \right|,\ \lambda_h(t) = \frac{1}{A_h(t)} \frac{dA_h(t)}{dt},$$
$$E_{h_{0,1}}(t) = \int_{-\infty}^{\infty} h_{0,1}(x,t) dx. \tag{27}$$

We first show the results for $P_e = 10^2$, $a = b = 0.1$, $\alpha = 2$. Figure 8(a) shows the amplification ratio, A_h, for this case for varying wavenumbers k. $A_h < 1$ for the range of k and times shown, and decreases in time except for $k = 1$ where there is a slight increase in A_h at around $t = 10$ followed by a slow decrease. Moreover, the rate of decrease in A_h increases with k. We next consider the effect of increasing Pe. Figure 8(b) shows A_h for $P_e = 10^4$, $a = b = 10$, $\alpha = 2$, for varying $k = 0 - 10, 15, 20, 30$. At very early times, the growth rate $\lambda_h > 0$ for the range of k shown, since A_h increases at these times. Moreover, perturbations with the largest values of k grow the fastest. This is consistent with the analysis above which shows that the that the perturbations grow as the wavenumber k increases when the necessary condition on the base state h_0 displaying a fluid ridge near its leading edge is satisfied (see Figs. 6(c) and 7(a)). We observe the maximum in A_h to be attained at $t \approx 50$ for $k = 0 - 20$. Moreover, the maximum in A_h increases for k in this range. A_h begins to decrease for $t > 50$. The rate of decrease, λ_h, is more prominent for very large k (see Fig. 8(b) for $k = 15, 20$). The gradual decay of the fluid ridge in the base state is the stabilising influence for these values of k. For lower values of k, the long time decay in A_h

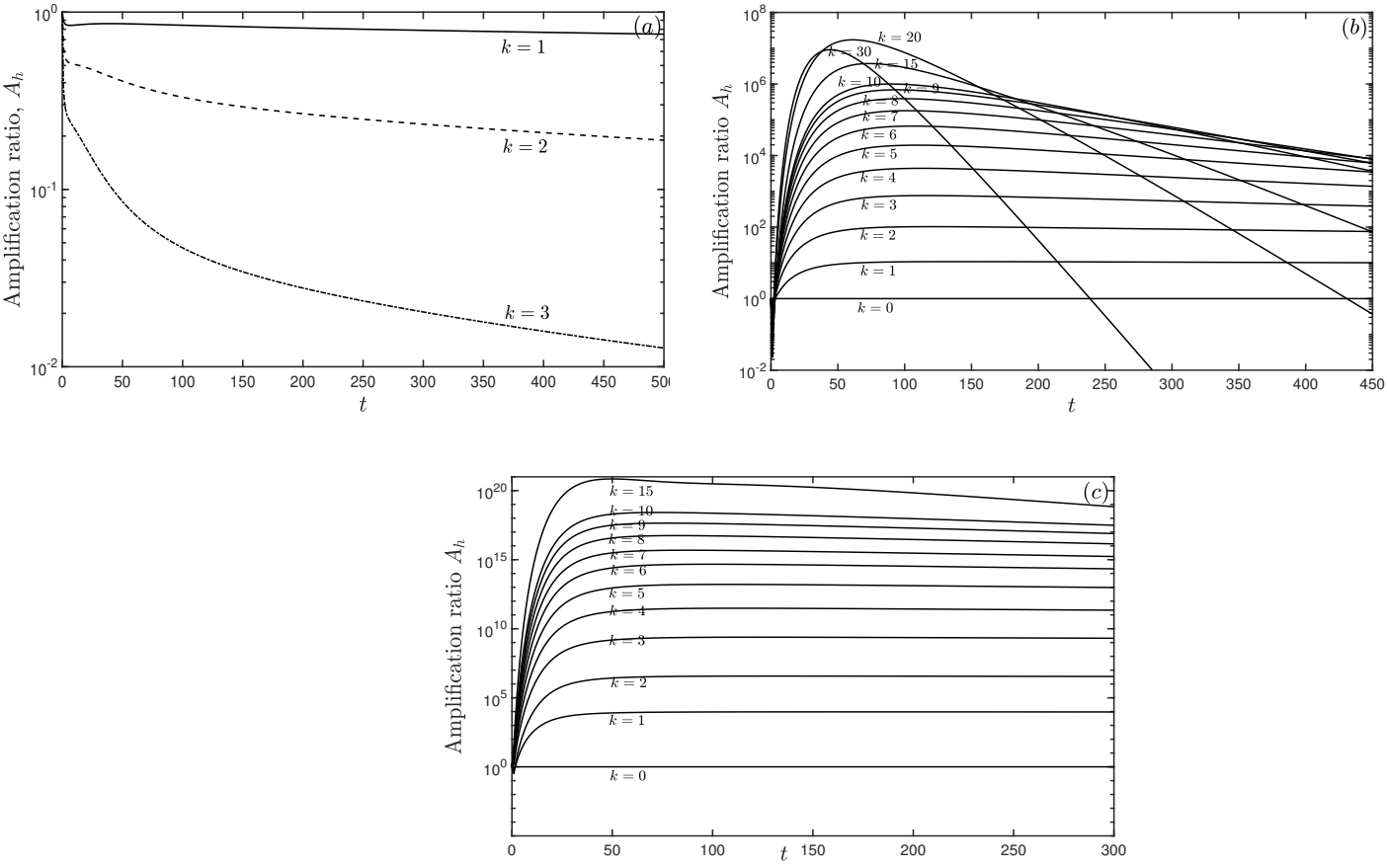

Figure 8: The amplification ratio A_h for varying wavenumber k. The parameter values are: (a) $P_e = 10^2$, $a = b = 0.1$, $\alpha = 2$, (b) $P_e = 10^4$, $a = b = 10$, $\alpha = 2$, and (c) $P_e = 10^4$, $a = b = 10$, $\alpha = 4$.

is very slow (see Fig. 8(b) for $k \leq 10$). For even larger values of k, the initial growth of the instability saturates earlier than that corresponding to $k = 0 - 20$. We observe that for $k = 30$ in Fig. 8(b), the maximum in A_h is attained earlier and is lower than that corresponding to $k = 20$. The subsequent rate of decrease, λ_h, is also greater than that corresponding to $k = 20$. This suggests that the stabilizing influence as the fluid ridge in the base state gradually decays is much stronger for these values of k (as observed for $k = 30$). Figure 8(c) show the effect of increasing α for varying k, the other parameters are the same as in the case above. The amplification ratios and growth rates are much higher for larger α. This is again consistent with the necessary condition for instability to occur; the fluid ridge in the base state h_0 is more amplified for larger α and also persists for a longer time, which explains the enhanced amplification and growth rates. Moreover, increasing α also increases the viscosity contrast at the leading edge, enhancing the instability.

We note the following parameter variations without showing the results here. Increasing the inclination angle accentuates the instability via a more pronounced ridge. Similarly, introducing a source flux, $Q_{s_0} > 0$, creates a sustained fluid ridge prolonging the instability. In conclusion, the linear stability analysis shows the existence of the fluid ridge and the viscosity contrast between the ridge and the leading edge of the front to be necessary for linear instability. When this is satisfied, the shortest transverse waves (large k) grow fastest at early times and decay fastest at late times, stabilized by the decay in height of the initial fluid ridge and the viscosity contrast. Generally, surface tension would also stabilize the larger wavenumbers, but is not important for the problem considered here. Extensional viscous stresses omitted in the lubrication theory here could also be important for stabilization at large k[27].

B. Nonlinear stability

In this section, we examine the nonlinear transverse stability of Eq. (22) to small-amplitude transverse perturbations superimposed on a base state flow and temperature field using two-dimensional numerical simulations. We seek 2π-periodic solutions (2-periodic used in computations) in y for $-L \leq x \leq L$ and $0 \leq y \leq 2\pi$, where L

is the length of the computational domain in the x direction. We introduce initial localised periodic transverse perturbations around the leading edge of the front of a given wavenumber of the form:

$$[h(x,y,t=0),\theta(x,y,t=0)] = [h_0(x),\theta_0(x)] + \sum_{i=1}^{M} A_i \cos(k_i \pi y) e^{[-K(x-x_f)^2]}, (x,y) \in [-L_1,L_2]\times[-1,1],$$

where k_i is the wavenumber and A_i is the amplitude of the 2-periodic transverse mode, K controls the width of the localised perturbation which is applied at $x = x_f$, the location of the leading edge of the front. We are interested in investigating and simulating the existence of a fingering instability when the front spreads to a much longer distance. In this scenario, the order of a wavelength in the transverse y direction is much smaller than the spreading length.

The evolution equation for $h(x,y,t)$ and $\theta(x,y,t)$ given by Eq. (22) are solved numerically by the method of lines using finite-difference schemes similar to those described in §III A. The boundary conditions are: $h \to \delta$ and $\theta_x \to 0$ as $x \to \pm\infty$. In all the results shown below, we fix the source flux $Q_{s_0} = 0$ (constant volume spreading), the precursor thickness, $\delta = 10^{-3}$ and $S = 1$ (inclined plane at an angle of approximately 6^o). The typical domain length considered in the simulations is $[-2,16]\times[-1,1]$ and the mesh sizes are $\Delta x = 0.02-0.03$ and $\Delta y = 0.02$. This resulted in a system of $O(10^5)$ differential-algebraic equations at each time step which were solved in MATLAB (Release 2013a, The MathWorks Inc., Natick, Massachusetts, United States) using the stiff ODE solver *ode15i*. We have tested the accuracy and convergence of our numerical scheme by reproducing the planar solutions shown in §III A for a variety of parameter values.

We have also tested the nonlinear simulations with the corresponding linear stability analysis results, when the initial perturbation is sufficiently small. The linear stability equations, Eqs. (24), are scaled appropriately to compare with the 2-periodic nonlinear simulations. We compare the amplification ratios at early times for perturbations with a prescribed wavenumber k. In these comparisons, the amplitude and width of the perturbation $A = 10^{-3}, K = 10^2$, respectively, are chosen to be the same for both sets of calculations. Figure 9(a,b,c) compares the amplification ratios, $A_h(y=0,t)$ (labelled 'nonlinear') and $A_h(t)$ (labelled 'linear'), at early times for varying wavenumbers k. $A_h(y=0,t)$ is calculated based on $h_1(x,y=0,t) = h(x,y=0,t) - h_0(x,t)$. The parameter values are: $P_e = 10^2$, $a = b = 0.1$, $\alpha = 2$ (Fig. 9(a)), $P_e = 10^2$, $a = b = 0.1$, $\alpha = 6$ (Fig. 9(b)), and $P_e = 10^4$, $a = b = 10$, $\alpha = 4$ (Fig. 9(c)). Depending on the parameter values, the results agree quantitatively at very early - early times as illustrated in Figs. 9$(a-c)$. For the stable case shown in Fig. 9(a), $A_h < 1$ in both the linear and nonlinear results and decreases in time with the rate of decrease in A_h increasing with k (consistent with Fig. 8(a)). The rate of decrease in A_h for the nonlinear simulations, however, slows down as time progresses in comparison to the exponential decay in the linear stability results. For the unstable case shown in Fig. 9(c), we observe that A_h decreases with k at early times in both the linear and nonlinear results. Following this, A_h begins to increase with k as the perturbations grow. The linear stability results show exponential growth with k at these times (consistent with Fig. 8(b,c)). However, the nonlinear simulations show the modes to saturate (with the higher modes saturating earlier) and gradually decrease as time progresses; eventually the $k = 1$ mode becomes the dominant wavenumber. For the unstable case shown in Fig. 9(b), the linear and nonlinear results agree quantitatively at very early times when A_h decreases with k. As time progresses, the agreement is at best qualitative for this case even when the perturbations are small. As the perturbations grow, the growth rates of the $k \geq 2$ modes slowly decrease in time, and the $k = 1$ mode eventually becomes the dominant wavenumber.

In order to explain the differences between the linear and nonlinear results it is instructive to compare the weakly nonlinear terms in h given by $2k^2h_0^2h_1^2/\mu_0$ and $-2k^2h_0^3\mu_1/(3\mu_0^2)$, with the corresponding linear term, $k^2h_0^3h_1/(3\mu_0)$ (see Eq. (24a)). We measure the amplification of the ratio of the weakly nonlinear versus linear terms which can be written as: $\int_{-\infty}^{\infty} 6h_1/h_0\, dx$ and $\int_{-\infty}^{\infty} 2\alpha\theta_1 dx$. These are evaluated at $y = 0$ from the nonlinear simulations (labelled 'nonlinear') and the corresponding linear stability analysis (labelled 'linear'), and shown in Figs. 9(d,e,f) for $k = 1$. The values are normalized with the corresponding values at $t = 0$. For the case considered in Figs. 9(f), there is not much difference between the linear and nonlinear results at early times, suggesting that the weakly nonlinear evolution is well captured by the linear stability analysis (Figs. 9(c)). In contrast, Fig. 9(e) shows the nonlinear results to diverge from the linear results except at very early times, reflected in the difference between the linear and nonlinear amplification seen in Fig. 9(b). Assuming that the base state $h_0 \sim t^{-\beta}$ $(0 < \beta < 1)$ (Fig. 3(f)) and the perturbation $h_1 \sim e^{\lambda t}$ $(\lambda > 0)$, then $\int_{-\infty}^{\infty} 6h_1/h_0\, dx \sim t^{\beta}e^{\lambda t}$. The amplification at early times $\sim t^{\beta}$ which is due to the decay of the base state (rather than growth in perturbations); at later times the exponential growth in h_1 dominates the amplification of the weakly nonlinear terms. The time at which this transition occurs can be estimated as $t \sim (\sqrt{\beta} - \beta)/\lambda$ (corresponding to an inflection point). Depending on the values of β and λ (which depend on the system parameters and the wavenumber), this linear-to-weakly nonlinear transition can occur at early times (Fig. 9(f)) or only at very early times (Fig. 9(e)). For the stable case, $\int_{-\infty}^{\infty} 6h_1/h_0\, dx \sim t^{\beta}e^{-\lambda t}$. In this case, the amplification at early times is due to the decaying base state; at later times the weakly nonlinear terms gradually decay compared to the exponential decay in the linear term (Fig. 9(d)). The transition from linear-weakly nonlinear in this case occurs at $t \sim \beta/\lambda$.

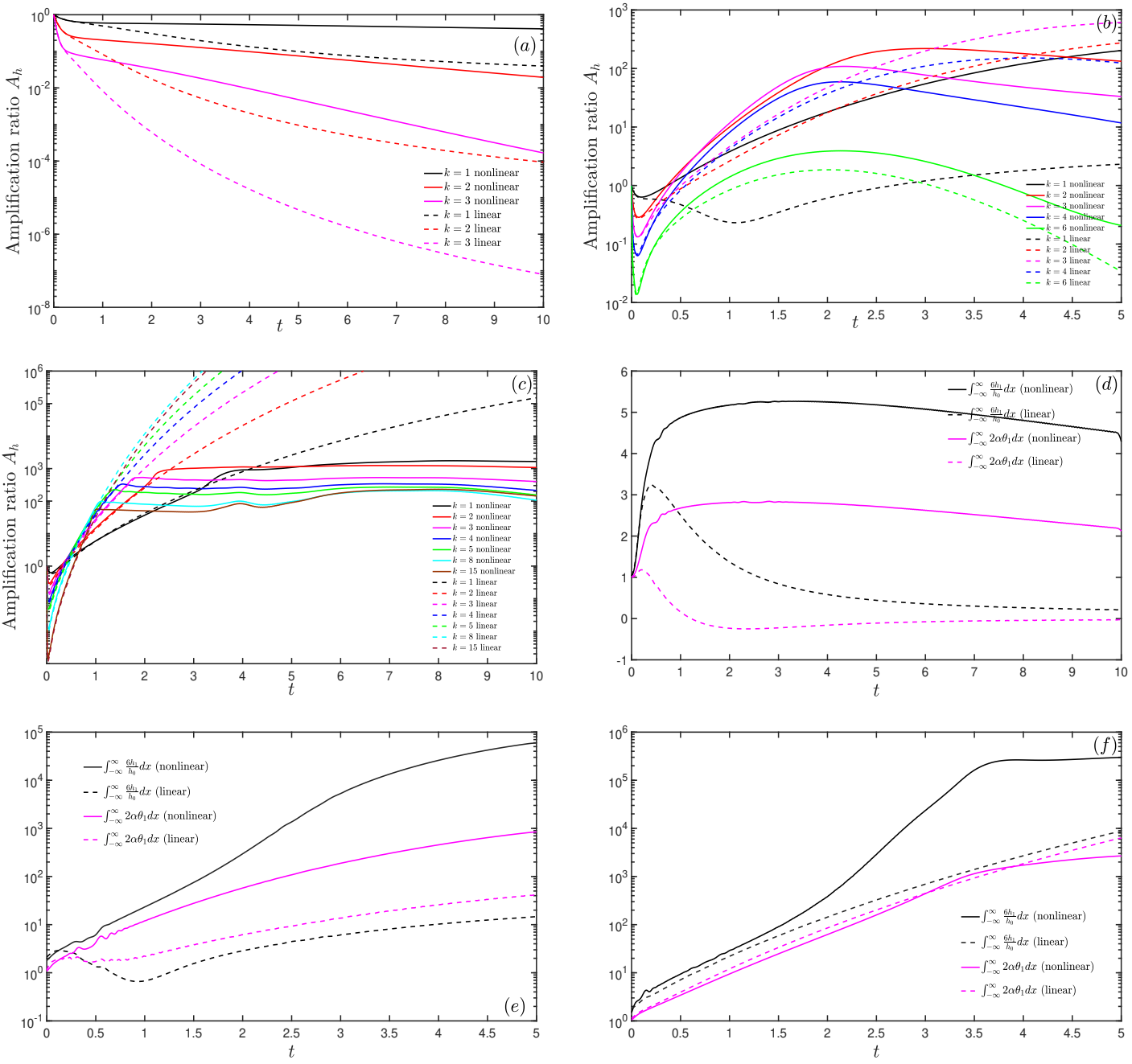

Figure 9: (a, b, c). Comparison of the amplification ratios from the nonlinear simulations, $A_h(y = 0, t)$ (labelled 'nonlinear'), and $A_h(t)$ from the linear stability analysis (labelled 'linear'), for varying wavenumbers. (d, e, f). Comparison of the amplification of the ratio between the weakly nonlinear and linear terms at $y = 0$ from the nonlinear simulations and from the linear stability analysis, for $k = 1$ (see text for details). The amplification ratios are normalized with the corresponding values at $t = 0$. The parameter values are: (a, d) $P_e = 10^2$, $a = b = 0.1$, $\alpha = 2$, (b, e) $P_e = 10^2$, $a = b = 0.1$, $\alpha = 6$, and (c, f) $P_e = 10^4$, $a = b = 10$, $\alpha = 4$.

We confirm that the weakly nonlinear terms are stabilizing, contributing to the nonlinear saturation and slow decrease in the amplification ratios in the nonlinear simulations (Figs. 9(a, b, c)).

The slow dominance of the $k = 1$ mode over the other wavenumbers observed in Fig. 9(b, c) is further explored in the nonlinear simulations shown below. Figure 10 shows the contour plot of the evolution of $h(x, y, t)$ (a, c, e) and $\theta(x, y, t)$ (b, d, f) for times, $t = 0, 10, 30$, respectively, with $Pe = 10^2$, $\alpha = 6$, $a = b = 0.1$. The base

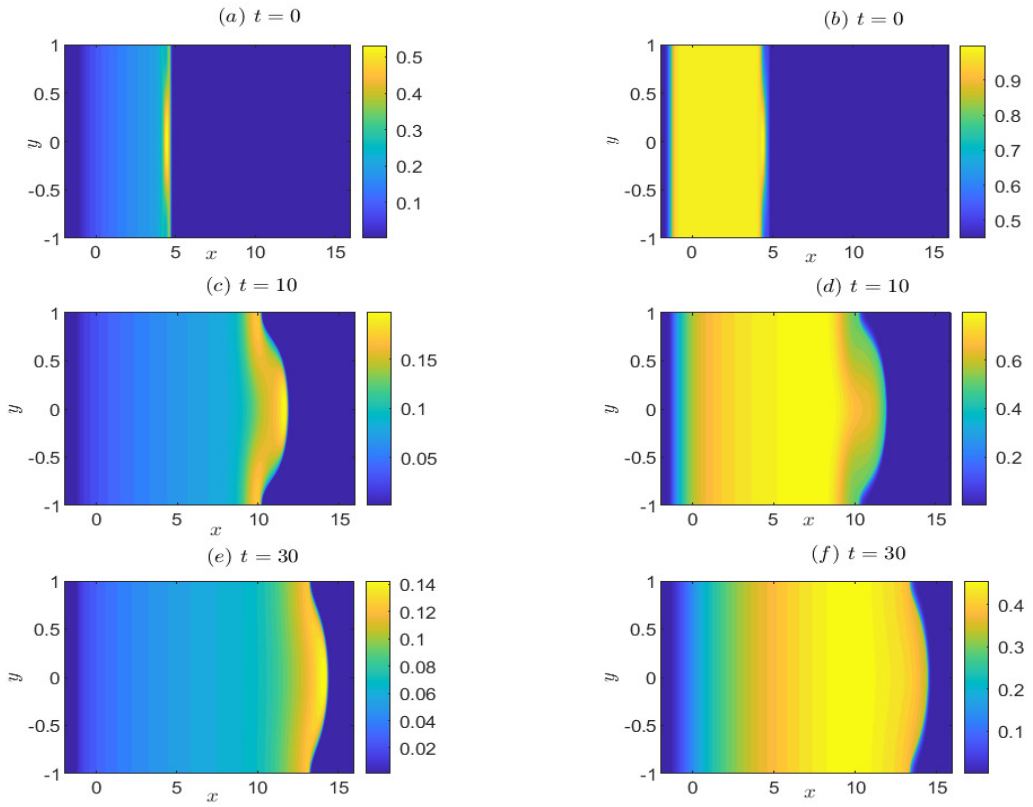

Figure 10: Contour plot of the evolution of $h(x, y, t)$ (a, c, e) and $\theta(x, y, t)$ (b, d, f) for time, $t = 0$ (a, b), $t = 10$ (c, d) and $t = 30$ (e, f) with $S = 1$ (inclination angle approximately 6^o), $Pe = 10^2$, $\alpha = 6$, $a = b = 0.1$, $k = 1$ and $A = 0.02$.

state $h_0(x)$ for this case has a slumped dome-shaped profile with a fluid ridge (Fig. 10(a)) and a sufficiently large gradient in $\theta_0(x)$ exists at the dome's leading edge (Fig. 10(b)), both precursors for linear instability to be initiated. We impose a transverse perturbation with a single wavenumber $k = 1$ and amplitude $A = 0.02$ on both $(h, \theta)_0(x)$ (see Fig. 10(a, b)). We observe clearly in this case that both base states lose their stability to a fingering instability in the transverse direction. The instability mechanism is as follows. A perturbation of the fluid ridge making it higher at a point along with an increase in temperature due to the perturbation in θ makes it move faster due to the horizontal component of gravity, and the perturbation will grow. This manifests itself at the dome's leading edge as a protruding finger (Fig. 10(c)), hotter in the middle and cooler at the edges (Fig. 10(d)). However, transverse diffusion (controlled by Pe)) moves heat away from the centre to the edges cooling down the emerging finger (Fig. 10(f)). This combined with the decay in the base state slows down the finger gradually weakening it. A much weaker instability (smaller growth rate compared to $k = 1$) is observed for $k = 2$ and the perturbations decay to zero for $t \geq 10$ (see Fig. 9(b)). A similar behaviour is observed for $k \geq 3$ (see Fig. 9(b)).

We next consider the evolution of $h(x, y, t)$ and $\theta(x, y, t)$ for intermediate values of Pe, represented by $Pe = 10^4$. Figure 11 shows the contour plot of the time evolution of $h(x, y, t)$ (left panels) and $\theta(x, y, t)$ (right panels), with $Pe = 10^4$, $\alpha = 4$, $a = b = 10$ and $k = 1$. We impose a transverse perturbation with wavenumber $k = 1$ and amplitude $A = 0.02$ on both $h_0(x)$ and $\theta_0(x)$ (see Fig. 11(a, b)). We observe that the both the base states lose their stability to a fingering instability with a similar mechanism as in the previous case, except that instability is more localised around $y = 0$. This is due to transverse diffusion of heat being much weaker for larger Pe so the centre of the protruding finger loses heat (cools) much more slowly, allowing the finger to be sustained for a longer period of time. Figure 12 shows the evolution of $h(x, y, t)$ (left panels) and $\theta(x, y, t)$ (right panels) for the same parameter set, except $k = 2$. The fingering instability still exists for this wavenumber with a growth rate comparable to $k = 1$ (see Fig. 9(c)). Similar behaviour is observed for $k = 3$, except that the instability weakens in time (see Fig. 9(c)); results not shown here). The weaker transverse diffusion of heat promoting the finger is now offset by the stabilizing effect of the flow due to transverse diffusion, i.e., $Q^{(y)}$ in Eq. (A6), which is potentially

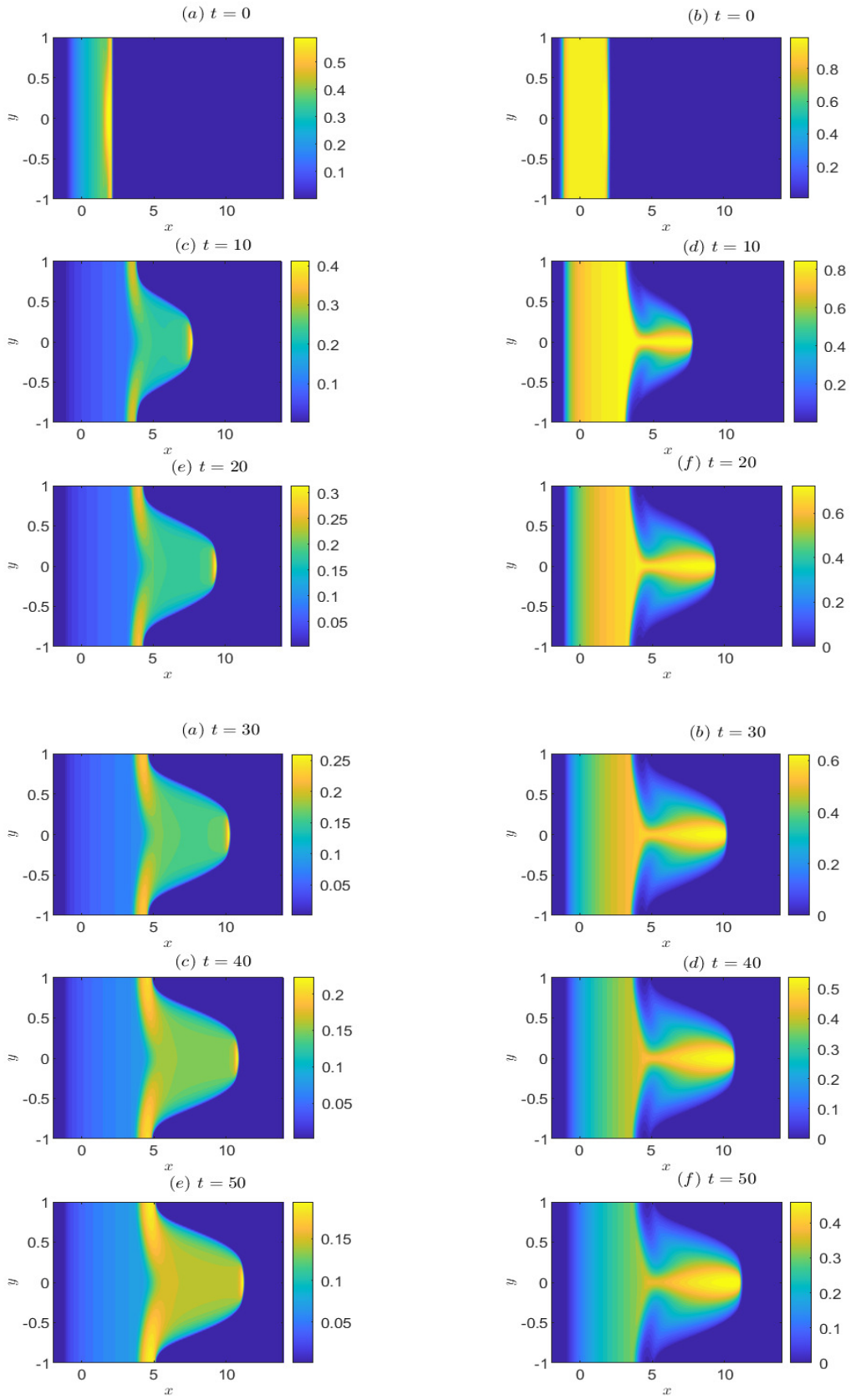

Figure 11: Contour plot of the time evolution of $h(x, y, t)$ (left panels) and $\theta(x, y, t)$ (right panels), with $S = 1$ (inclination angle approximately 6^o), $Pe = 10^4$, $\alpha = 4$, $a = b = 10$, $k = 1$ and $A = 0.02$.

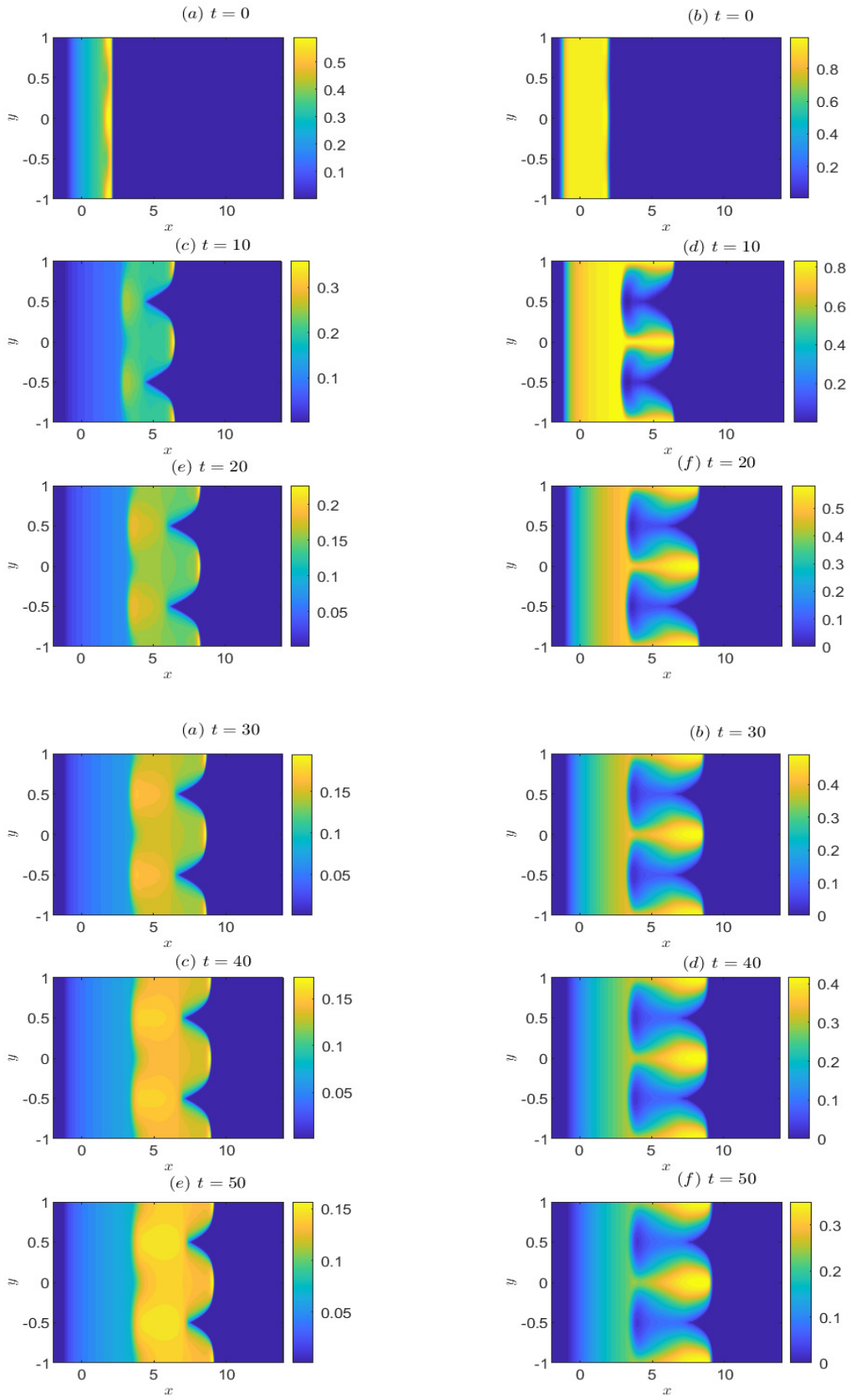

Figure 12: Contour plot of the time evolution of $h(x, y, t)$ (left panels) and $\theta(x, y, t)$ (right panels), with $S = 1$ (inclination angle approximately 6^o), $Pe = 10^4$, $\alpha = 4$, $a = b = 10$, $k = 2$ and $A = 0.02$.

enhanced at higher wavenumbers. A similar behaviour is observed for $k \geq 3$ (see Fig. 9(c)).

VI. DISCUSSION

We used the thin film equation coupled to an advection-diffusion equation for the temperature to investigate the spreading and cooling of a hot Newtonian liquid dome down an inclined plane. We considered non-isothermal conditions for the reduced Péclet number, $Pe_r = O(1)$, including a temperature-dependent viscosity and heat loss due to cooling at the free surface and substrate. Our results highlighted a key feature during the spreading process, namely the preferential cooling near the dome's leading edge where the rate of heat loss is maximum. The extent of this cooling ranged from a *collar* of colder liquid near the dome's leading edge (for intermediate Pe_r) to one where the temperature isotherms became almost vertical across the dome (for low Pe_r).

Our results advance beyond previous work on cooling spreading domes on horizontal surfaces[15–18]. We showed that the cooler more viscous collar near the dome's leading edge holds back less viscous hotter fluid behind it; the enhanced mobility of the hotter fluid due to both the lower viscosity and inclination of the substrate resulted in the formation of a localized fluid ridge at the leading edge of the dome overriding a spreading slumped dome. The fluid ridge played an important role in the nonlinear dynamics and fingering instability of the contact line at the dome's leading edge. This structure is absent for spreading on a horizontal substrate. Although the above scenario also exists here, the absence of extra mobility does not allow the creation of the fluid ridge.

The main highlight of this study is that the relatively weak instability examined for cooling spreading domes on horizontal surfaces[15–18] can be made more powerful by placing the fluid on an inclined surface. The extent to which the fluid ridge and temperature gradient (and corresponding viscosity contrast) near the dome's leading edge necessitate the initiation of the fingering instability is revealed using a linear stability analysis combined with numerical simulations. The necessary conditions combined with the parameter mapping shown in Fig. 5 provided the threshold conditions for predicting *a priori* whether the fingering will occur or not. Previous stability studies[17,18] for cooling spreading domes on horizontal surfaces identified the thermo-viscous instability mechanism elucidated in §V B but they could only predict a very weak instability, possibly due to the absence of a fluid ridge in this case. The instability is damped out eventually for constant volume spreading, however, introducing a constant flux of hot liquid through the vent sustained the fingering instability (results not shown here).

The viscous fingering instability observed in this work is similar to viscous banding instability first identified by Kowal[14], except that the viscous banding here is dynamically generated due to temperature variations along the viscous-gravity current. While the viscous banding linear instability mechanism reported by Kowal[14] is directly related to the free surface slope discontinuity across the intrusion front, no fluid ridge is observed. This may be due to the sharp discontinuity in viscosity assumed at the intrusion front, whereas in our work there is a length-scale $O(Pe^{-1/3})$ over which the discontinuity in viscosity is smoothed allowing for a ridge solution to exist across the intrusion front. Moreover, the fluid ridge played a crucial role in the linear instability through destabilizing buoyancy forces with the instability enhanced for increasing wavenumbers (§V A and Fig. 8(b,c)), stabilizing at later times as the ridge dissipates. This is in contrast to Kowal[14] where the buoyancy forces stabilize the linear instability at large wavenumbers.

There are limitations to this study. The linear stability analysis and numerical simulations were performed using $Pe_r = O(1)$ values, which pushes the boundaries of the $Pe_r \ll 1$ (vertically isothermal) asymptotic theory on which they are based on. Although we have not made a direct comparison between $Pe_r \ll 1$ and $Pe_r = O(1)$ (vertically non-isothermal) results, the nonlinear dynamics displayed by the $Pe_r = O(1)$ numerical results are captured and their underlying physical mechanisms preserved. Based on this we can be confident about extending the asymptotic theory to the range of intermediate Pe_r values considered here. We would need to perform the stability analysis including the three-dimensional temperature field to investigate much higher values of Pe_r. This will be considered in future work.

We have only investigated Newtonian rheology. In reality, such flows exhibit non-Newtonian and viscoplastic behaviour, and the yield stress can be strongly dependent on temperature[17,18]. The interaction between the so-called pseudo-plug region (which starts forming from the surface) and surface cooling is important when the cooling boundary layer at the surface advances into the plug region, otherwise the plug *shields* the dome from cooling. As part of the future work, we would need to extend our model to include temperature-dependent non-Newtonian effects and their influence on cooling.

A key ingredient missing in this work is phase transition due to solidification at both the free surface (surface crust) and the substrate. Previous models have considered spreading under the influence of solidification of the underlying substrate[28,29]; a bi-viscosity model[15] has also been used as a proxy to model a very viscous surface crust. The crust can directly affect the dynamics by contributing additional mechanical forces, e.g., a tensile restraining force[30]. The formation of the liquid ridge would depend on the competition between the force pushing the hotter liquid behind the front against the restoring force applied by the surface crust. Hence, the interaction between the surface crust and the underlying hot liquid flow would need to be taken into account.

ACKNOWLEDGEMENTS

This work was a part of Ghanim Algwauish's PhD research at Keele University[31]. Ghanim gratefully acknowledges financial support from the Ministry of Higher Education and Scientific Research and Mosul University in Iraq.

DECLARATION OF INTERESTS

No conflicts of interest:: The authors report no conflict of interest.

DATA AVAILABILITY STATEMENT

The data that support the findings of this study are available from the corresponding author upon reasonable request.

Appendix A: Derivation of the evolution equation in Eqs. (19,20)

Using the lubrication approximation, the leading order equations governing the flow can be written as:

$$u_x + v_y + w_z = 0, \tag{A1a}$$
$$-p_x + \partial_z \tau_{xz} + S = 0, \tag{A1b}$$
$$-p_y + \partial_z \tau_{yz} = 0, \tag{A1c}$$
$$-p_z - 1 = 0, \tag{A1d}$$
$$\tau_{xz} = \tau_{yz} = p = 0,$$
$$h_t + u h_x + v h_y = w, \quad \text{at} \quad z = h(x,t), \tag{A1e}$$
$$u = 0,\ v = 0,\ w = w_s(x,y,t), \quad \text{at} \quad z = 0. \tag{A1f}$$

Integrating Eq. (A1d) with respect to z between $z = 0$ and $z = h$, and using the boundary condition for p in Eq. (A1e) gives $p = h(x,t) - z$. Integrating Eq. (A1b) with respect to z between $z = 0$ and $z = h$, and using the boundary condition for τ_{xz} in Eq. (A1e) and p above gives $\tau_{xz}(x,z) = (S - h_x)(h - z)$. Integrating Eq. (A1c) with respect to z between $z = 0$ and $z = h$, and using the boundary condition for τ_{yz} in Eq. (A1e) and p above gives $\tau_{yz}(x,z) = (-h_y)(h - z)$. Using Eqs. (13),(15) and the shear stresses τ_{xz}, and τ_{yz}, we obtain the leading order shear rate,

$$u_z = (S - h_x)\frac{(h-z)}{\mu(\theta)}, \quad v_z = (-h_y)\frac{(h-z)}{\mu(\theta)}. \tag{A2}$$

Integrating Eq. (A2) with respect to z and using the boundary conditions for u and v in Eq. (A1f), we obtain

$$u(x,y,z,t) = (S - h_x)\int_0^z \frac{(h-z')}{\mu(\theta)} dz', \tag{A3a}$$
$$v(x,y,z,t) = (-h_y)\int_0^z \frac{(h-z')}{\mu(\theta)} dz'. \tag{A3b}$$

Using the continuity equation, Eq. (A1a), and the boundary condition for w in Eq. (A1f), gives

$$w(x,y,z,t) = -\int_0^z u_x dz' - \int_0^z v_y dz' + w_s(x,y,t). \tag{A4}$$

Now, the leading order liquid flux through a cross-section can be written as:

$$Q^{(x)}(x,y,t) = \int_0^h (h-z) u_z dz,$$
$$Q^{(y)}(x,y,t) = \int_0^h (h-z) v_z dz. \tag{A5}$$

Using the expression for u_z, and v_z above, we obtain

$$Q^{(x)}(x,y,t) = (S - h_x)\int_0^h \frac{(h-z)^2}{\mu(\theta)} dz,$$
$$Q^{(y)}(x,y,t) = (-h_y)\int_0^h \frac{(h-z)^2}{\mu(\theta)} dz. \tag{A6}$$

Integrating the continuity equation, Eq. (A1a), using the boundary conditions in Eq. (A1f) and substituting into the kinematic boundary condition in Eq. (A1e), one obtains the depth-averaged evolution equation for h:

$$h_t + Q^{(x)}_x + Q^{(y)}_y = w_s. \tag{A7}$$

Using the expressions for $Q^{(x)}$, $Q^{(y)}$ from above, we can write the evolution equation for $h(x,y,t)$ as:

$$h_t = \nabla.\left(\left[\int_0^h \frac{(h-z)^2}{\mu(\theta)} dz\right]\nabla h\right) - S\left(\int_0^h \frac{(h-z)^2}{\mu(\theta)} dz\right)_x + w_s, \tag{A8}$$

where $w_s(x,y,t)$ is given by Eq. (17).

Appendix B: Derivation of the reduced model for $Pe = O(1)$

We consider the asymptotic limit, where the Péclet number, $Pe = O(1)$, so that the reduced Péclet number, $Pe_r = O(\epsilon^2)$. We also impose the heat transfer coefficients $(a,b) = O(\epsilon^2)$. In this limit, let $\theta = \theta_0(x,y,z,t) + \epsilon^2\theta_2(x,y,z,t) + \ldots$ Substituting into Eq. (21) gives to leading order:

$$\theta_{0_{zz}} = 0, \quad \theta_{0_z} = 0 \quad \text{at} \quad z = 0 \quad \text{and} \quad z = h(x,y,t). \tag{B1}$$

This implies $\theta_0 = \theta_0(x,y,t)$. Hence, $\theta = \theta_0(x,y,t) + \epsilon^2\theta_2(x,y,z,t) + \ldots$.

Substituting this in Eq. (21) gives

$$Pe\left[\theta_{0t} + u\theta_{0x} + v\theta_{0y}\right] = \left[\theta_{2zz} + \theta_{0xx} + \theta_{0yy}\right], \tag{B2a}$$
$$\theta_{2z} = h_x\theta_x + h_y\theta_{0y} - a\theta_0, \quad \text{at} \quad z = 0, \tag{B2b}$$
$$\theta_{2z} = Pe(\theta_0 - 1)w_s + b(\theta_0 - \theta_{0s}), \quad \text{at} \quad z = h(x,y,t). \tag{B2c}$$

Integrating Eq. (B2a) from $z=0$ to $z=h$, and using the boundary conditions Eqs. (B2b,B2c), we obtain

$$h_x\theta_{0x}+h_y\theta_{0y}-a\theta-[Pe(\theta_0-1)w_s+b(\theta_0-\theta_{0s})]= Pe(h\theta_{0t}+\theta_{0x}\int_0^h udz+\theta_{0y}\int_0^h vdz)h\theta_{0xx}-h\theta_{0yy}. \tag{B3}$$

Dropping the subscripts, the leading order temperature field is thus gives by

$$\theta_t+[\frac{Q^{(x)}}{h}-\frac{h_x}{hPe}]\theta_x+[\frac{Q^{(y)}}{h}-\frac{h_y}{hPe}]\theta_y=\frac{1}{Pe}[\theta_{xx}+\theta_{yy}] -\frac{1}{hPe}[a\theta+b(\theta-\theta_s)]-\frac{w_s}{h}(\theta-1), \tag{B4}$$

where

$$Q^{(x)}=\frac{1}{3}\frac{h^3}{\mu(\theta)}(S-h_x),\quad Q^{(y)}=\frac{1}{3}\frac{h^3}{\mu(\theta)}(-h_y). \tag{B5}$$

Thus, the evolution equation for the free surface and the temperature field are given by:

$$h_t+Q_x^{(x)}+Q_y^{(y)}=w_s, \tag{B6a}$$

$$\theta_t+[\frac{Q^{(x)}}{h}-\frac{h_x}{hPe}]\theta_x+[\frac{Q^{(y)}}{h}-\frac{h_y}{hPe}]\theta_y=\frac{1}{Pe}[\theta_{xx}+\theta_{yy}] -\frac{1}{hPe}[a\theta+b(\theta-\theta_s)]-\frac{w_s}{h}(\theta-1), \tag{B6b}$$

$$Q^{(x)}=\frac{1}{3}\frac{h^3}{\mu(\theta)}(S-h_x),\quad Q^{(y)}=\frac{1}{3}\frac{h^3}{\mu(\theta)}(-h_y), \tag{B6c}$$

$$\mu(\theta)=e^{-\alpha\theta}, \tag{B6d}$$

$$w_s=[9Q_{s_0}Q_s(t)/16]\left[1-\left(\frac{x}{x_0}\right)^2\right]_+\left[1-\left(\frac{y}{y_0}\right)^2\right]_+. \tag{B6e}$$

Appendix C: Mapping $(x,z)\in[0,1]\times[0,h]$ to a Rectangular Domain $(x,z)\in[0,1]\times[0,1]$

In order to solve Eqs. (20),21a) numerically, it is instructive to map $(x,z)\in[0,1]\times[0,h]$ to a rectangular domain $(x,z)\in[0,1]\times[0,1]$. We apply the following change of variables:

$$\bar{x}=x,\quad \bar{z}=\frac{z}{h(x,t)},\quad \bar{t}=t. \tag{C1}$$

Using the chain rule, we can write

$$\frac{\partial}{\partial x}=\frac{\partial}{\partial\bar{x}}-\frac{\bar{z}h_{\bar{x}}}{h}\frac{\partial}{\partial\bar{z}},\quad \frac{\partial}{\partial z}=\frac{1}{h}\frac{\partial}{\partial\bar{z}}, \quad \frac{\partial}{\partial t}=\frac{\partial}{\partial\bar{t}}-\frac{\bar{z}h_{\bar{t}}}{h}\frac{\partial}{\partial\bar{z}}. \tag{C2}$$

Applying the above change of variables, the new set of transformed evolution equations for $h(\bar{x},\bar{t})$ and $\theta(\bar{x},\bar{z},\bar{t})$ can be written as:

$$h_{\bar{t}}+Q_{\bar{x}}=w_s, \tag{C3a}$$

$$Q=h^3(S-h_{\bar{x}})\int_{\bar{z}=0}^{\bar{z}=1}\frac{(1-\bar{z})^2}{\mu(\theta)}\,d\bar{z}, \tag{C3b}$$

$$w_s=\begin{cases}\frac{9}{16}Q_{s_0}Q_s(t)\left[1-(\bar{x}/\bar{x}_0)^2\right], & \bar{x}\le|\bar{x}_0|,\\ 0, & \text{otherwise},\end{cases} \tag{C3c}$$

$$\epsilon^2Pe[\theta_{\bar{t}}+u\theta_{\bar{x}}+(w-\bar{z}uh_{\bar{x}}-\bar{z}h_{\bar{t}})\frac{1}{h}\theta_{\bar{z}}]=\frac{1}{h^2}\theta_{\bar{z}\bar{z}}, \tag{C3d}$$

$$\theta_{\bar{z}}=\epsilon^2hPe(\theta-1)w_s+bh(\theta-\theta_s),\ \text{ at } \bar{z}=0, \tag{C3e}$$

$$\theta_{\bar{z}}=\frac{\epsilon^2hh_{\bar{x}}\theta_{\bar{x}}}{1+\epsilon^2\bar{z}h_{\bar{x}}^2}-\frac{ah\theta}{1+\epsilon^2\bar{z}h_{\bar{x}}^2},\ \text{ at } \bar{z}=1. \tag{C3f}$$

We need to determine the transformed velocity field, (u,w). In order to do this, the Eq. (A2) is first transformed and solved for horizontal velocity component which implies

$$u_{\bar{z}}=h^2(S-h_{\bar{x}})\frac{(1-\bar{z})}{\mu(\theta)}. \tag{C4}$$

Using the continuity equation in transformed variables gives

$$w_{\bar{z}}=\bar{z}h_{\bar{x}}u_{\bar{z}}-hu_{\bar{x}}. \tag{C5}$$

Integrating Eq. (C4) subject to $u=0$ on $\bar{z}=0$ gives

$$u(\bar{x},\bar{z},\bar{t})=h^2(S-h_x)\int_0^{\bar{z}}\frac{(1-\acute{z})}{\mu(\theta)}d\acute{z}, \tag{C6}$$

Substituting Eq. (C4) and (C6) into transformed continuity equation, we obtain

$$w_{\bar{z}}=h^2h_{\bar{x}}(S-h_{\bar{x}})\frac{\bar{z}(1-\bar{z})}{\mu(\theta)} -h\partial_{\bar{x}}\left(h^2(S-h_{\bar{x}})\int_0^{\bar{z}}\frac{(1-\acute{z})}{\mu(\theta)}d\acute{z}\right). \tag{C7}$$

Integrating with respect to $\bar{z}$ and using the condition $w=w_s$ on $\bar{z}=0$ implies

$$w(\bar{x},\bar{z},\bar{t})=h^2h_{\bar{x}}(S-h_{\bar{x}})\int_0^{\bar{z}}\frac{\acute{z}(1-\acute{z})}{\mu(\theta)} -h\partial_{\bar{x}}\left(h^2(S-h_{\bar{x}})\int_0^{\acute{z}}\left(\int_0^{\acute{\acute{z}}}\frac{(1-\acute{z})}{\mu(\theta)}d\acute{\acute{z}}\right)d\acute{z}\right)+w_s. \tag{C8}$$

The above equation can be simplified by changing the order of the integration. An integral of the form

$$\int_0^{\acute{z}}\int_0^{\acute{\acute{z}}}f(x,z,t)d\acute{z}d\acute{\acute{z}}, \tag{C9}$$

on interchanging the order of integration becomes

$$\int_0^{\acute{z}}\int_0^{\acute{\acute{z}}}f(x,z,t)d\acute{z}d\acute{\acute{z}}=\int_0^{\acute{z}}f(x,z,t)(z-\acute{z})d\acute{z}. \tag{C10}$$

Therefore Eq. (C8) can be written as:

$$w(\bar{x},\bar{z},\bar{t}) = h^2 h_{\bar{x}}(S-h_{\bar{x}})\int_0^{\bar{z}} \frac{\acute{z}(1-\acute{z})}{\mu(\theta)}d\acute{z}$$
$$- h\partial_{\bar{x}}\left(h^2(S-h_{\bar{x}})\int_0^{\bar{z}} \frac{(1-\acute{z})(\bar{z}-\acute{z})}{\mu(\theta)}d\acute{z}\right) + w_s. \quad \text{(C11)}$$

Appendix D: Geometric criterion to quantify the elevation of the fluid ridge

In order to quantify the elevated ridge near the flow front observed for intermediate values of Pe_r, it is instructive to plot the slope of the free surface h_x there. Figures 13(a,b) show h_x (dashed curves) at $t = 30$ near the flow front for $Pe_r = 10^2, 10^4$, respectively, corresponding to the free surface shape profiles $h(x, t = 30)$ (solid curves; time evolution shown in Fig. 3(c,d)). We observe that for $Pe_r = 10^2$ which exhibits an elevated ridge at the flow front during the evolution (solid curve in Fig. 13(a)), h_x has a prominent local maximum between the back edge and the main peak of the ridge (dashed curve in Fig. 13(a)). In contrast for $Pe_r = 10^4$, although a local maximum in h_x exists here (Fig. 13(b)), it is much less prominent compared to Fig. 13(a). The degree of elevation is quantified as follows. We observe a local minimum in h_x (dashed curves in Fig. 13(a,b)) where the curvature of h changes from concave down (in the bulk section of the dome) to concave up (at the back edge of the ridge).

A geometric criterion to quantify the elevation of the ridge is that the change in the local angle of elevation given by $\tan^{-1}(h_x|_{\max}) - \tan^{-1}(h_x|_{\min})$ should exceed a prescribed threshold value during the evolution. If this is the case, then the ridge is classified to be elevated.

REFERENCES

[1] A. Oron, S. H. Davis, and S. G. Bankoff, "Long-scale evolution of thin liquid films," Rev. Mod. Phy. **69**, 931–980 (1997).
[2] R. Craster and O. Matar, "Dynamics and stability of thin liquid films," Rev. Mod. Phys. **81**, 1131–1198 (2009).
[3] T. G. Myers, "Surface tension driven thin film flows," in *The Mechanics of Thin Film Coatings* (Wiley, 1996).
[4] E. Boujo and M. Sellier, "Pancake making and surface coating: Optimal control of a gravity-driven liquid film," Phys. Rev. Fluids **4**, 064802 (2019).
[5] C. Journeau, F. Sudreau, J. Gatt, and C. Gérard, "Thermal, physico–chemical and rheological boundary layers in multi–component oxidic melt spreads," Int. J. Thermal Sci. **38**, 879–891 (1999).
[6] R. W. Griffiths, "The dynamics of lava flows," Annu. Rev. Fluid Mech. **32**, 477–518 (2000).
[7] J. F. Nye, "Mechanics of glacier flow," J. Glaciol. **2**, 82–93 (1952).
[8] A. M. Johnson, *Physical Processes in Geology* (Freeman, San Francisco, 1970).
[9] H. E. Huppert, "Gravity currents: a personal perspective," J. Fluid Mech. **554**, 299–322 (2006).
[10] H. Bleile and S. Rodgers, "Marine coatings," in *Encyclopedia of Materials: Science and Technology*, edited by K. J. Buschow, R. W. Cahn, M. C. Flemings, B. Ilschner, E. J. Kramer, S. Mahajan, and P. Veyssière (Elsevier, Oxford, 2001) pp. 5174–5185.
[11] S. Diniega, S. E. Smrekar, S. Anderson, and E. Stofan, "The influence of temperature-dependent viscosity on lava flow dynamics," J. Geophys. Res.: Earth Surface **118**, 1516–1532 (2013).
[12] C. Ancey, "Plasticity and geophysical flows: A review," J. Non-Newtonian Fluid Mech. **142**, 4–35 (2007).
[13] P. G. Saffman and G. Taylor, "The penetration of a fluid into a porous medium or hele-shaw cell containing a more viscous liquid," Proc. R. Soc. Lond. A **245**, 312–329 (1958).
[14] K. N. Kowal, "Viscous banding instabilities: non-porous viscous fingering," J. Fluid Mech. **926**, 926–946 (2021).
[15] J. R. King, D. S. Riley, and A. Sansom, "Gravity currents with temperature-dependent viscosity," Comput. Assist. Mech. Eng. Sci. **7**, 251–277 (2000).
[16] A. Sansom, J. R. King, and D. S. Riley, "Degenerate-diffusion models for the spreading of thin non-isothermal gravity currents," J. Eng. Maths **48**, 43–68 (2004).
[17] N. J. Balmforth and R. V. Craster, "Dynamics of cooling domes of viscoplastic fluid," J. Fluid Mech. **422**, 225–248 (2000).
[18] N. J. Balmforth, R. V. Craster, and R. Sassi, "Dynamics of cooling viscoplastic domes," J. Fluid Mech. **499**, 149–182 (2004).
[19] A. Sansom, *Spreading gravity currents with temperature–dependent viscosity*, Ph.D. thesis, University of Nottingham (2000).
[20] J. J. Wylie and J. R. Lister, "The effect of temperature-dependent viscosity on flow in a cooled channel with application to basaltic fissure eruptions," J. Fluid Mech. **305**, 239–261 (1995).
[21] G. D. Smith, *Numerical Solution of Partial Differential Equations: Finite Difference Methods*, 3rd ed. (Macmillan, 1985).
[22] K. W. Morton and D. F. Mayers, *Numerical Solution of Partial Differential Equations*, 2nd ed. (Cambridge University Press, 2005).
[23] J. R. Lister, "Viscous flows down an inclined plane from point and line sources," J. Fluid Mech. **242**, 631–653 (1992).
[24] L. Kondic, "Instabilities in gravity driven flow of thin fluid films," SIAM Rev. **45**, 95–115 (2003).
[25] B. D. Edmonstone, O. K. Matar, and R. V. Craster, "Flow of surfactant–laden thin films down an inclined plane," J. Engrg. Math. **50**, 141–156 (2004).
[26] N. J. Balmforth, A. S. Buridge, R. V. Craster, J. Salzig, and A. Shen, "Visco–plastic models of isothermal lava domes," J. Fluid Mech. **403**, 37–65 (2000).
[27] N. J. Balmforth, R. V. Craster, and C. Toniolo, "Interfacial instability in non–Newtonian fluid layers," Phys. Fluids **15**, 3370–3384 (2003).
[28] M. Bunk and J. R. King, "Spreading melts with basal solidification," Z. Angew. Math. Mech. **83**, 820–843 (2003).
[29] T. Myers, J. Charpin, and S. J. Chapman, "The flow and solidifiction of a thin fluid film on an arbitrary three-dimensional surface," Phys. Fluids **14**, 2788–2803 (2002).
[30] R. M. Iverson, "Lava domes modeled as brittle shells that enclose pressurized magma," in *Lava Flows and Domes: Emplacement Mechanisms and Hazard Implications*, edited by J. Fink (Springer, 1990) pp. 47–69.
[31] G. A. Algwauish, *The non-Newtonian and non-isothermal spreading of liquid domes using mathematical and numerical methods*, Ph.D. thesis, Keele University (2019).

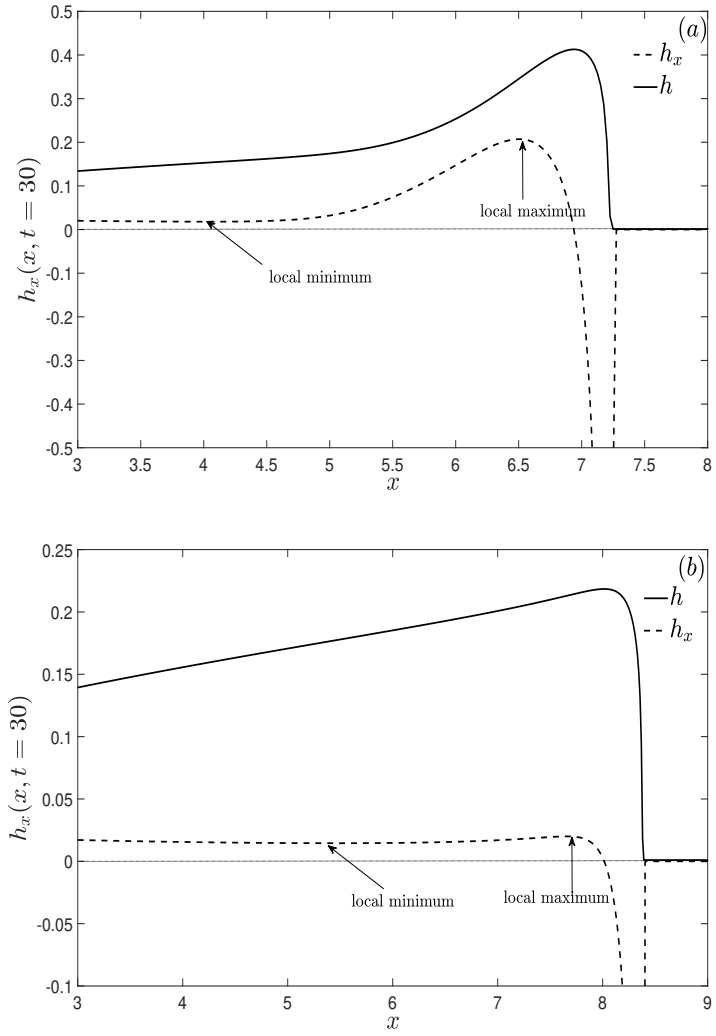

Figure 13: $h_x(x, t = 30)$ (dashed curves) corresponding to $h(x, t = 30)$ (solid curves) for (a) $Pe_r = 10^2$ and (b) $Pe_r = 10^4$. The parameter values are: $S = 1$ (plane inclined at 6^o), $\alpha = 2$, $Q_{s_0} = 0$, $\theta_s = 0$, $a = 0.02$ and $b = 0.03$.